Composite Vertical-Motion Patterns near North American Polar–Subtropical Jet Superposition Events

ANDREW C. WINTERS,[a] DANIEL KEYSER,[b] AND LANCE F. BOSART[b]

[a] *Department of Atmospheric and Oceanic Sciences, University of Colorado Boulder, Boulder, Colorado*
[b] *Department of Atmospheric and Environmental Sciences, University at Albany, State University of New York, Albany, New York*

(Manuscript received 2 May 2020, in final form 8 September 2020)

ABSTRACT: A polar–subtropical jet superposition is preceded by the development of a polar cyclonic potential vorticity (PV) anomaly at high latitudes and a tropical anticyclonic PV anomaly at subtropical latitudes. A confluent large-scale flow pattern can lead to the juxtaposition of these respective PV anomalies at middle latitudes, resulting in the addition of the nondivergent circulations induced by each PV anomaly and an increase in upper-tropospheric wind speeds at the location of jet superposition. Once these PV anomalies become juxtaposed, vertical motion within the near-jet environment facilitates the advection and diabatic redistribution of tropopause-level PV, and the subsequent formation of the steep, single-step tropopause structure that characterizes a jet superposition. Given the importance of vertical motion during the formation of jet superpositions, this study adopts a quasigeostrophic (QG) diagnostic approach to quantify the production of vertical motion during three types of jet superposition events: polar dominant, eastern subtropical dominant, and western subtropical dominant. The diagnosis reveals that the geostrophic wind induced by polar cyclonic QGPV anomalies is predominantly responsible for QG vertical motion in the vicinity of jet superpositions. The QG vertical motion diagnosed from the along-isotherm component of the **Q** vector, which represents the vertical motion associated with synoptic-scale waves, is dominant within the near-jet environment. The QG vertical motion diagnosed from the across-isotherm component of the **Q** vector, which represents the vertical motion associated with frontal circulations in the vicinity of the jet, is subordinate within the near-jet environment, but is relatively more important during eastern subtropical dominant events compared to polar dominant and western subtropical dominant events.

KEYWORDS: North America; Potential vorticity; Synoptic climatology; Vertical motion; Frontogenesis/frontolysis; Jets

1. Introduction

Polar–subtropical jet superpositions represent a type of synoptic-scale environment conducive to high-impact weather (Winters and Martin 2014, 2016, 2017; Handlos and Martin 2016; Christenson et al. 2017; Winters et al. 2020). The development of a jet superposition is conceptualized by Winters and Martin (2017; their Fig. 2) and Winters et al. (2020; their Fig. 1) using a potential vorticity (PV) framework. The forthcoming discussion of this conceptual model, adapted here in Fig. 1, parallels that in Winters et al. (2020). Prior to jet superposition, the large-scale flow pattern features a polar cyclonic PV anomaly at high latitudes and a tropical anticyclonic PV anomaly at subtropical latitudes (Fig. 1a). Polar cyclonic PV anomalies often develop in association with coherent tropopause disturbances (e.g., Hakim 2000; Pyle et al. 2004) or tropopause polar vortices (e.g., Cavallo and Hakim 2009, 2010, 2012, 2013), whereas tropical anticyclonic PV anomalies often develop in association with the transport of tropical, low-PV upper-tropospheric air toward middle latitudes via low-latitude troughs (e.g., Morgan and Nielsen-Gammon 1998; Iskenderian 1995; Roundy et al. 2010; Fröhlich et al. 2013; Winters and Martin 2016) and the diabatic erosion of upper-tropospheric PV that accompanies widespread latent heating (e.g., Lee and Kim 2003; Agusti-Panareda et al. 2004; Ahmadi-Givi et al. 2004; Son and Lee 2005; Grams et al. 2011, 2013; Grams and Archambault 2016; Winters and Martin 2017).

The upper-tropospheric jets are closely related to the positions of polar cyclonic and tropical anticyclonic PV anomalies within the aforementioned conceptual model. In particular, the polar jet (e.g., Palmén and Newton 1948; Namias and Clapp 1949; Newton 1954; Palmén and Newton 1969, 197–200; Keyser and Shapiro 1986, 458–461; Shapiro and Keyser 1990) is located equatorward of the polar cyclonic PV anomaly, while the subtropical jet (e.g., Starr 1948; Loewe and Radok 1950; Yeh 1950; Koteswaram 1953; Mohri 1953; Koteswaram and Parthasarathy 1954; Sutcliffe and Bannon 1954; Krishnamurti 1961; Riehl 1962) is located poleward of the tropical anticyclonic PV anomaly (Fig. 1a). A jet superposition occurs when the initially separate polar cyclonic and tropical anticyclonic PV anomalies become juxtaposed at middle latitudes. The idealized vertical cross section in Fig. 1c reveals that jet superpositions are associated with a steep, single-step pole-to-equator tropopause structure, rather than the two-step tropopause structure that characterizes the vertical cross section in Fig. 1b through separate polar and subtropical jets. Jet superpositions are also marked by strong baroclinicity in the upper troposphere and lower stratosphere, and strong wind speeds

Denotes content that is immediately available upon publication as open access.

Corresponding author: Andrew C. Winters, andrew.c.winters@colorado.edu

DOI: 10.1175/MWR-D-20-0140.1

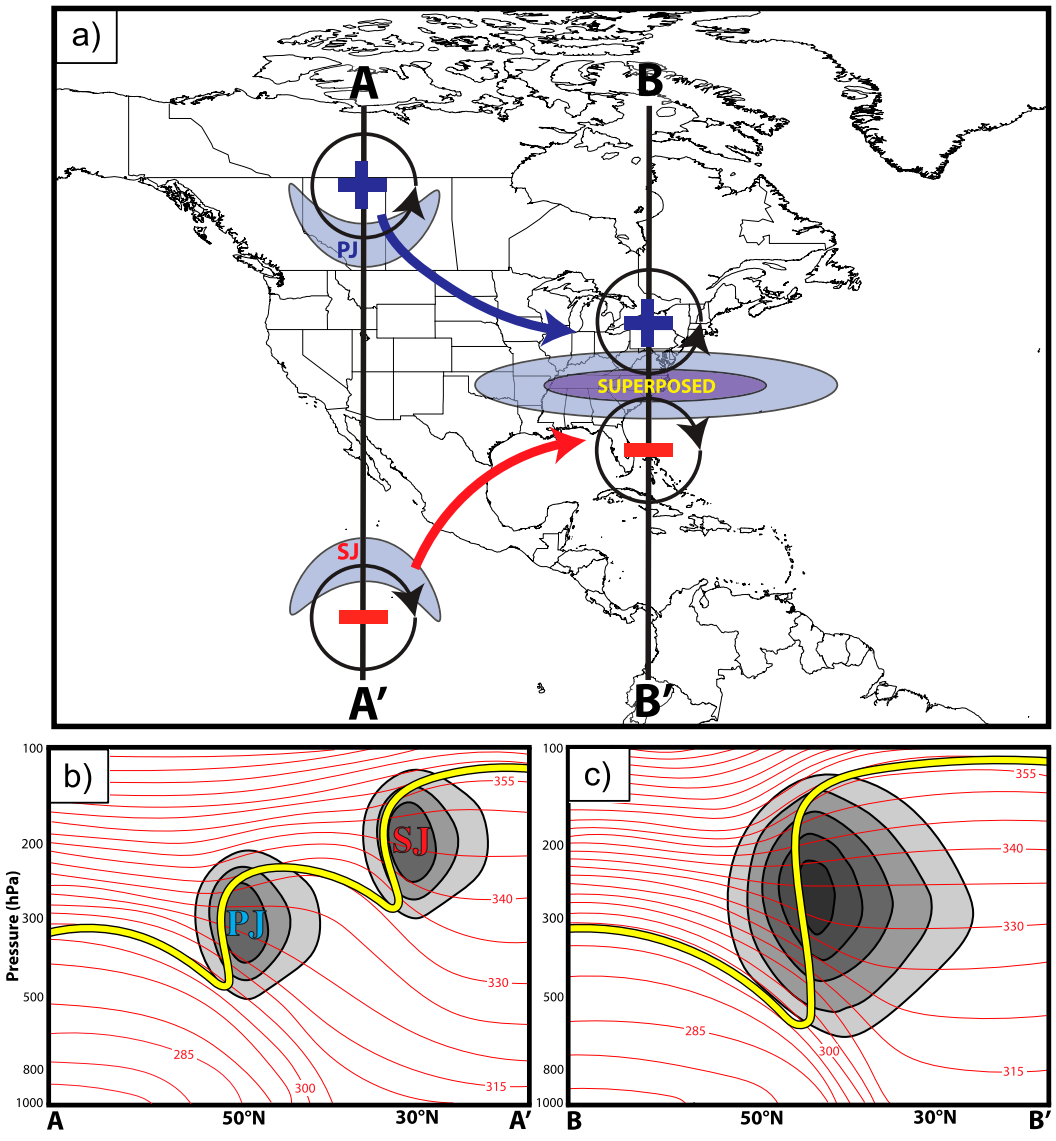

FIG. 1. (a) Conceptual model summarizing the development of a jet superposition. The plus sign and the minus sign correspond to a polar cyclonic and tropical anticyclonic PV anomaly, respectively, with the blue and red arrows indicating the movement of each PV anomaly toward middle latitudes. The purple fill corresponds to isotachs, with the darker shade of purple identifying stronger wind speeds. (b) Idealized cross section along A–A′, as indicated in (a), through a separate polar jet (PJ) and subtropical jet (SJ). Wind speed (gray shading with darker shades of gray identifying stronger wind speeds), potential temperature (red lines every 5 K), and the 2-PVU contour (thick yellow line). (c) As in (b), but for the idealized cross section B–B′, as indicated in (a), through a jet superposition. Figure and caption are adapted from Winters et al. (2020; their Fig. 1).

that result from the addition of the nondivergent circulations induced by each respective PV anomaly (Fig. 1c).

The nature by which polar cyclonic and tropical anticyclonic PV anomalies interact prior to a jet superposition varies across events (Winters and Martin 2016). To characterize this variability, Winters et al. (2020) conducted a climatological analysis of North American jet superposition events by classifying events in the National Centers for Environmental Prediction Climate Forecast System Reanalysis (CFSR; Saha et al. 2010) based on the extent to which the polar and subtropical jets deviated from their respective climatological locations to form a superposition. ''Polar dominant'' events were classified as those events in which the polar jet superposes with the subtropical jet near the climatological location of the subtropical jet, while ''subtropical dominant'' events were classified as those events in which the subtropical jet superposes with the polar jet near the climatological location of the polar jet. Whereas polar dominant events often develop near the U.S.

Gulf Coast and the U.S.–Mexico border, subtropical dominant events preferentially develop on the eastern and western coasts of North America (Winters et al. 2020; their Fig. 4). The latter observation motivated Winters et al. (2020) to consider a separate eastern and western category of subtropical dominant events.

Across all jet superposition event types, Winters et al. (2020) determined that the three-dimensional divergent circulation within the near-jet environment strongly influences the development of the steep, single-step tropopause structure that characterizes a superposition. In particular, latent heating associated with moist ascent in the near-jet environment influences the development of a steep, single-step tropopause structure during both subtropical dominant event types via the diabatic redistribution of upper-tropospheric PV on the equatorward side of the jet (Winters et al. 2020; their Figs. 10a and 13a). The three-dimensional divergent circulation also acts to steepen the slope of the tropopause mechanically during both subtropical dominant event types via negative PV advection at the level of the dynamic tropopause. During polar dominant events, however, these two processes are located well downstream of the location of jet superposition and do not directly influence the formation of a steep, single-step tropopause structure (Winters et al. 2020; their Fig. 6). The presence of descent beneath the jet-entrance region at the time of jet superposition is a similarity across all jet superposition event types (Figs. 2a,c,e). This descent facilitates positive PV advection in the vicinity of the tropopause height minimum (Figs. 2b,d,f), and contributes to the formation of a steep, single-step tropopause structure during all event types via the downward advection of high-PV stratospheric air. Considered together, the influence of vertical motion during the production of each jet superposition event type motivates further investigation into the dynamical processes responsible for the production of vertical motion during jet superpositions.

Of particular interest is a desire to determine the relative influence that polar cyclonic and tropical anticyclonic PV anomalies have on the production of vertical motion during each event type. A PV framework provides an effective approach for such an investigation. Namely, knowledge of the PV distribution, suitable balance and boundary conditions, and a reference temperature profile permit a calculation of the mass and wind fields attributable to that PV distribution using PV inversion (e.g., Hoskins et al. 1985, 883–885; Thorpe 1985; Robinson 1988; Holopainen and Kaurola 1991; Davis and Emanuel 1991). In turn, the vertical-motion pattern associated with the calculated mass and wind fields can be determined using an ω equation that is consistent with the balance condition used to perform the aforementioned PV inversion. The application of PV inversion has shown considerable utility for investigating a variety of characteristics of the atmospheric flow pattern, such as flow in the middle atmosphere (e.g., Robinson 1988), the planetary-scale tropospheric flow (e.g., Holopainen and Kaurola 1991), surface cyclogenesis (e.g., Davis and Emanuel 1991; Black and Dole 1993; Hakim et al. 1996; Nielsen-Gammon and Lefevre 1996), tropopause folding (e.g., Wandishin et al. 2000), and upper-tropospheric blocking events (e.g., Breeden and Martin 2018, 2019).

The proposed application of PV inversion in this study is similar to that employed by Winters and Martin (2017) for a jet superposition event that coincided with the 18–20 December 2009 Mid-Atlantic Blizzard. In that case, Winters and Martin (2017) determined that the three-dimensional divergent circulation induced by PV anomalies residing along the polar jet waveguide contributed more to the formation of a steep, single-step structure than the three-dimensional divergent circulation induced by PV anomalies residing along the subtropical jet waveguide. While only applicable to a single jet superposition event, the results from Winters and Martin (2017) provide a foundation from which to examine whether a similar conclusion can be drawn for each jet superposition event type and across a large number of cases.

The configuration of the 500-hPa vertical-motion pattern in the vicinity of jet superpositions at the time of jet superposition also differs across the three event types (Figs. 2a,c,e), which suggests that the dynamical mechanisms responsible for the production of vertical motion may vary based on the event type. In particular, the vertical-motion pattern features cellular structures during polar dominant events, whereas the vertical-motion pattern features banded structures that parallel the jet axis during both subtropical dominant event types. The $\mathbf{Q}$ vector (e.g., Hoskins et al. 1978; Hoskins and Pedder 1980), and its partition into an along-isotherm $\mathbf{Q}_s$ and an across-isotherm $\mathbf{Q}_n$ component (e.g., Keyser et al. 1988, 1992; Sanders and Hoskins 1990; Martin 1999, 2006, 2014; Hecht and Cordeira 2017; Kenyon et al. 2020), provides a diagnostic framework for examining the vertical-motion pattern in the vicinity of jet superpositions. In this framework, the divergence of $\mathbf{Q}_s$ is characterized by a cellular pattern and represents quasigeostrophic (QG) forcing for vertical motion associated with synoptic-scale waves (e.g., Sanders and Hoskins 1990; their Fig. 4). The divergence of $\mathbf{Q}_n$ is characterized by a banded pattern that parallels areas of enhanced baroclinicity and represents QG forcing for vertical motion associated with frontal circulations in the vicinity of the jet (e.g., Sanders and Hoskins 1990; their Figs. 5 and 6).

It is hypothesized that the cellular structure of the vertical-motion pattern observed during polar dominant events (Fig. 2a) is driven predominantly by the presence of an amplified upper-tropospheric flow pattern. Conversely, the banded structure of vertical motion during both subtropical dominant event types (Figs. 2c,e) suggests that across-front ageostrophic circulations arising due to frontogenesis make a comparatively larger contribution to the vertical-motion pattern during both subtropical dominant event types compared to polar dominant events. A determination of the extent to which vertical motion in the near-jet environment can be attributed to frontal circulations is also of interest given that the development of anomalously strong baroclinicity is a leading characteristic of jet superpositions.

The forthcoming study expands upon prior work into the production of vertical motion in the vicinity of upper-level jet-front systems (e.g., Schultz and Doswell 1999; Lang and Martin 2010, 2012, 2013; Martin 2014) by investigating the processes that facilitate the formation of a steep, single-step tropopause structure across a large sample of jet superposition events.

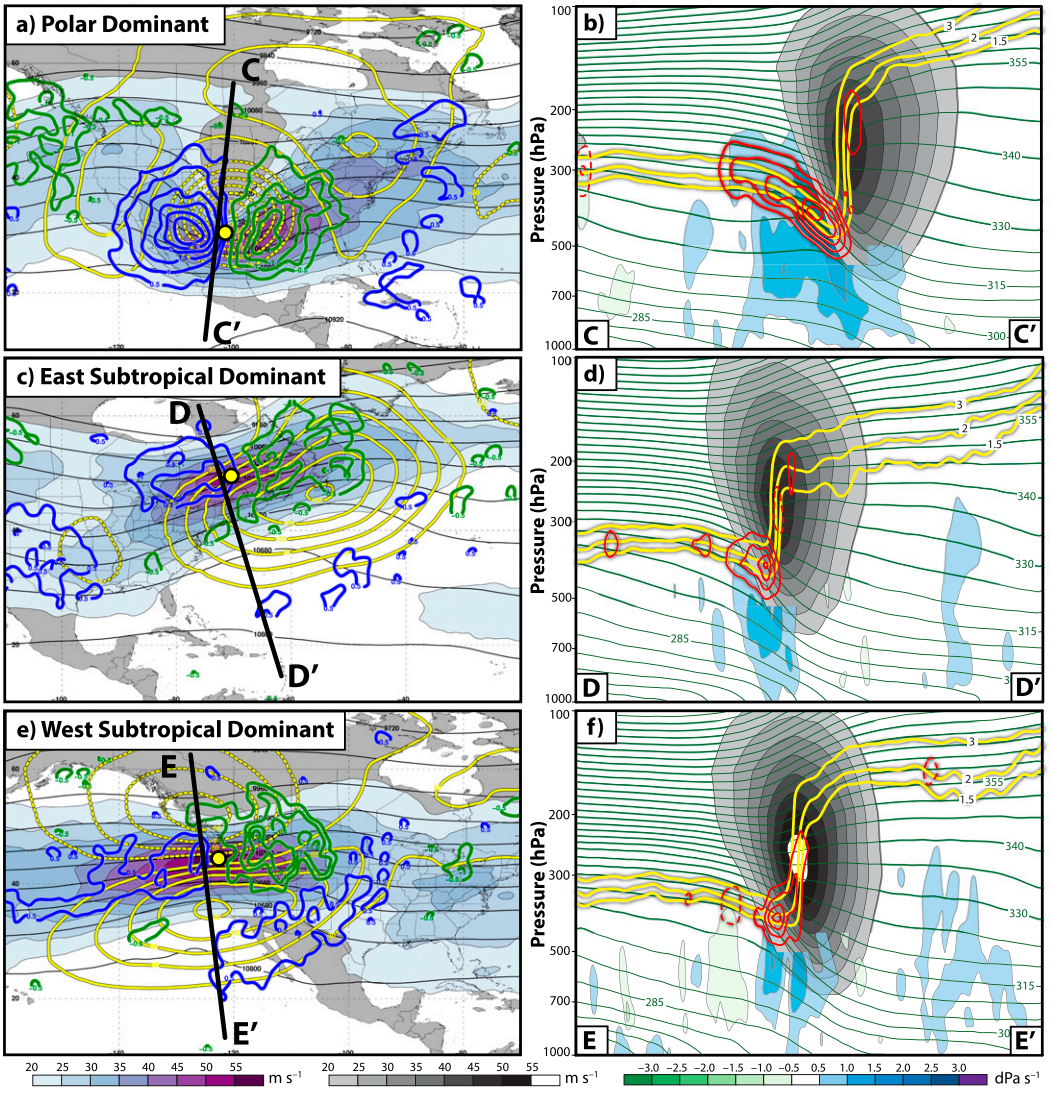

FIG. 2. (left) Composite 250-hPa geopotential height (black solid lines every 120 m), 250-hPa geopotential height anomalies (yellow lines every 30 m, solid when positive and dashed when negative), 250-hPa wind speed (shaded according to the legend; m s^{-1}), and 500-hPa vertical motion (contoured every 0.5 dPa s^{-1} in green for ascent and blue for descent) at the time of superposition for (a) polar dominant, (c) eastern subtropical dominant, and (e) western subtropical dominant jet superposition events. (right) Composite potential temperature (green lines every 5 K), wind speed (gray shading according to the legend; m s^{-1}), the 1.5-, 2-, and 3-PVU contours (yellow lines), PV advection by the three-dimensional divergent circulation (red lines every 0.5×10^{-5} PVU s^{-1}, solid when positive and dashed when negative), and vertical motion (shaded according to the legend; dPa s^{-1}) for (b) the cross section along C–C′, as indicated in (a), (d) the cross section along D–D′, as indicated in (c), and (f) the cross section along E–E′, as indicated in (e). Figure and caption are adapted from Winters et al. (2020; their Figs. 5, 7b, 8, 10b, 11, 13b).

The remainder of this study is structured as follows. Section 2 summarizes the jet superposition event classification scheme developed by Winters et al. (2020). Section 3 determines the fraction of the vertical-motion pattern during each jet superposition event type that can be attributed to polar cyclonic and tropical anticyclonic PV anomalies. Section 4 investigates the extent to which the vertical-motion pattern during each event type is associated with the divergence of the along-isotherm and across-isotherm components of the **Q** vector, and section 5 summarizes the results of this study.

2. Jet superposition event identification and classification

This study utilizes data at 6-h intervals from the CFSR (Saha et al. 2010) with 0.5° horizontal grid spacing and 50-hPa vertical grid spacing between 1000 and 50 hPa during

November–March 1979–2010. This study also utilizes 326 North American jet superposition events identified by Winters et al. (2020) in the CFSR during the same time period. Jet superpositions are identified in Winters et al. (2020) as those grid columns in the CFSR that feature (i) a strong horizontal PV gradient within both the 315–330- and 340–355-K layers (i.e., representing the formation of a steep, single-step tropopause structure) and (ii) a 400–100-hPa vertically integrated wind speed in excess of 30 m s^{-1}. North American jet superposition events are identified as those analysis times that rank in the top 10% in terms of the number of grid columns characterized by a jet superposition within the domain, 10°–80°N and 140°–50°W. For further detail on the jet superposition identification scheme and the procedures used to compile jet superposition events, the reader is referred to Winters et al. (2020, section 2a). The methods used to classify jet superposition events into event types are identical to Winters et al. (2020) and are reproduced below given their relevance to this study. The forthcoming text describing these methods is derived from Winters et al. (2020) with minor modifications.

Jet superposition event classification scheme

The location of each jet superposition event in Winters et al. (2020) is described by a latitude–longitude centroid that is calculated from an average of the latitude and longitude of all grid columns characterized by a jet superposition at the time the polar and subtropical jets first become superposed. The locations of the event centroids are subsequently used to classify events into event types based on the degree to which the polar and subtropical jets deviate from their respective climatological locations to form a jet superposition. The climatological location of the polar jet waveguide at an analysis time (e.g., 0000 UTC 1 January) is calculated by averaging the position of the 2-PVU (1 PVU = 10^{-6} K kg^{-1} m^2 s^{-2}) contour on the 320-K surface at 24-h intervals within a 21-day window centered on that analysis time during all years of the study period. The climatological position of the subtropical jet waveguide is determined similarly using the 350-K surface.

The event classification scheme compares the position of each event centroid against the climatological locations of the polar and subtropical jet waveguides at the start of an event. "Polar dominant" events ($N = 80$; Fig. 3a) are defined as those events in which an observation of 2 PVU at the location of the event centroid represents a standardized PV anomaly > 0.5 on the 320-K surface and a standardized PV anomaly > -0.5 on the 350-K surface. "Subtropical dominant" events ($N = 129$; Fig. 3b) are defined as those events in which an observation of 2 PVU at the location of the event centroid represents a standardized PV anomaly < 0.5 on the 320-K surface and a standardized PV anomaly < -0.5 on the 350-K surface.

Since subtropical dominant events are primarily focused on the eastern or western coast of North America (Winters et al. 2020; their Fig. 4c), subtropical dominant events are partitioned into an "eastern" ($N = 76$) and a "western" category ($N = 53$) based off the position of each event centroid relative to 96°W. The 117 events not classified as polar or subtropical dominant events are classified as "hybrid" events and represent a mutual deviation of both jets from their climatological locations. The focus of this study is to examine the vertical-motion patterns associated with polar dominant and subtropical dominant events, given that these events lie at opposite ends of the spectrum of the types of PV anomaly interactions that comprise jet superpositions. Consequently, hybrid events will not be considered in this study. Composite analyses are constructed for polar dominant, eastern subtropical dominant, and western subtropical dominant events within the domain, 10°–80°N and 150°E–10°W, following the methodology outlined in Winters et al. (2020, section 4), and a Gaussian

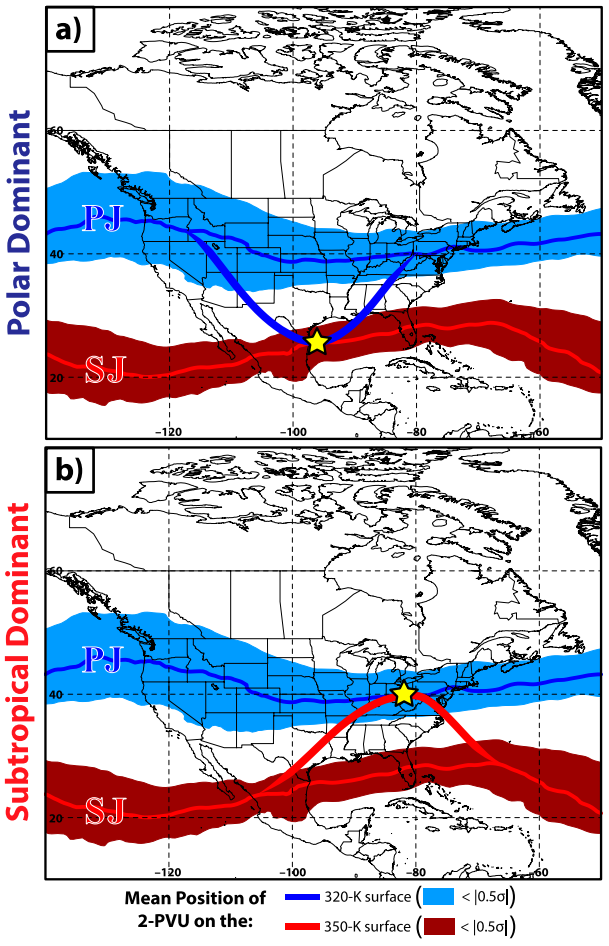

FIG. 3. The mean position of the 2-PVU contour on the 320- and 350-K surfaces at 0000 UTC 1 Jan is indicated by the thin blue line and thin red line, respectively, as a proxy for the position of the polar jet (PJ) and subtropical jet (SJ) waveguide. Shaded areas bounding each mean 2-PVU contour indicate locations at which an observation of 2 PVU on that particular isentropic surface would represent a standardized PV anomaly with a magnitude less than 0.5. A hypothetical deviation of the 2-PVU contour from its mean position on the 320-K surface during the formation of a (a) polar dominant jet superposition event (yellow star) is indicated by the thick blue contour. (b) As in (a), but for a subtropical dominant event. A hypothetical deviation of the 2-PVU contour from its mean position on the 350-K surface during the formation of a subtropical dominant event is indicated by the thick red contour. Figure and caption adapted from Winters et al. (2020; their Fig. 2).

smoother with 10 × 10 points is applied to all composite variables prior to performing the calculations described in sections 3 and 4.

3. The influence of polar cyclonic and tropical anticyclonic PV anomalies

a. *QGPV inversion*

This study adopts a QG approach, which defines the QGPV q associated with each jet superposition event type via the following equation (e.g., Charney and Stern 1962; Hoskins et al. 1985, 911–915):

$$q = f + \frac{1}{f_o}\nabla^2\phi + f_o\frac{\partial}{\partial p}\left(\frac{1}{\sigma_r}\frac{\partial\phi}{\partial p}\right), \tag{1}$$

where f is the latitudinally varying Coriolis parameter, f_o is a constant Coriolis parameter ($10^{-4}\,s^{-1}$), and $\nabla^2 = (\partial^2/\partial x^2, \partial^2/\partial y^2)$ is the two-dimensional Laplacian operator on an isobaric surface. The static stability coefficient $[\sigma_r = -(\alpha_r/\Theta_r)(\partial\Theta_r/\partial p)]$ is horizontally homogenous, where α_r and Θ_r are the specific volume and potential temperature, respectively, on an isobaric surface within an arbitrary reference atmosphere. The reference atmosphere is chosen to be the *U.S. Standard Atmosphere, 1976* in this study, and ϕ is defined as the difference between the composite geopotential Φ associated with a particular jet superposition event type and the reference geopotential Φ_r, such that $\phi = \Phi - \Phi_r$.

Although individual jet superposition events can be characterized by Rossby numbers of order 1 (Winters and Martin 2014, 2016, 2017), useful information can be obtained from QGPV inversion, so long as the QGPV distribution agrees qualitatively with the structure of the full Ertel PV (e.g., Davis 1992b; Hakim et al. 1996). To this point, Figs. 4a–c reveal that the distributions of 300-hPa QGPV [scaled by $-g(\partial\Theta_r/\partial p)$] and 300-hPa Ertel PV are strongly correlated[1] and qualitatively similar across all event type composites at the time of jet superposition. Prior applications of QGPV inversion to the synoptic-scale flow pattern (e.g., Holopainen and Kaurola 1991; Black and Dole 1993; Hakim et al. 1996; Nielsen-Gammon and Lefevre 1996; Wandishin et al. 2000; Breeden and Martin 2018, 2019) provide additional confidence in the utility of QGPV inversion for investigating jet superposition environments.

The QGPV q distribution can be partitioned into a mean QGPV q_m and an additional n discrete categories that group together subsets of the perturbation QGPV q' that are of similar origin or dynamical significance, such that $q = q_m + q' = q_m + \sum_{i=1}^{n} q_i'$. Table 1 lists the criteria used to partition the QGPV distribution during polar dominant, eastern subtropical dominant, and western subtropical dominant events. The mean QGPV q_m is determined for each event type by constructing a composite of the climatological mean geopotential Φ_m on all calendar days for which a jet superposition was observed for that event type. The difference between the composite climatological mean geopotential and the reference geopotential ($\phi_m = \Phi_m - \Phi_r$) is substituted into (1) to calculate q_m for each event type as follows:

$$q_m = f + \frac{1}{f_o}\nabla^2\phi_m + f_o\frac{\partial}{\partial p}\left(\frac{1}{\sigma_r}\frac{\partial\phi_m}{\partial p}\right). \tag{2}$$

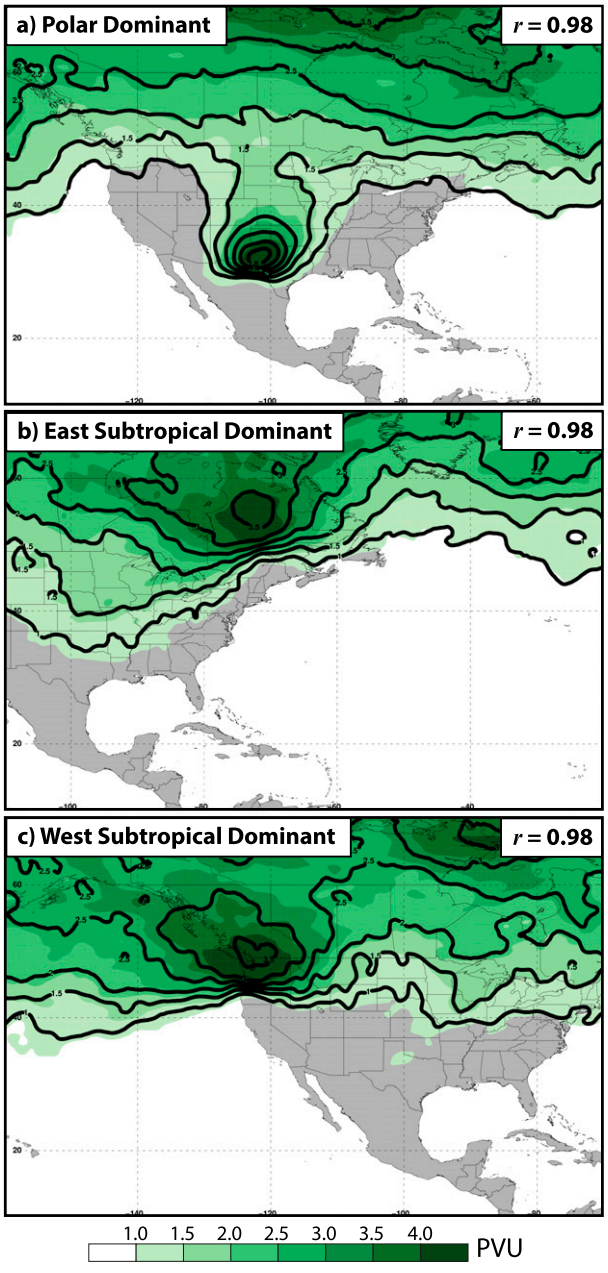

FIG. 4. 300-hPa Ertel PV (green shading according to the legend; PVU) and 300-hPa QGPV [scaled by $-g(\partial\Theta_r/\partial p)$; black lines every 0.5 PVU above 1 PVU] for (a) polar dominant, (b) eastern subtropical dominant, and (c) western subtropical dominant events at the time of jet superposition. The value in the top right of each panel indicates the spatial correlation between the 300-hPa Ertel PV and 300-hPa QGPV for each event type.

[1] Correlations between the QGPV and Ertel PV are greater than 0.95 on each isobaric level.

TABLE 1. The classification scheme used to partition the QGPV during polar dominant, eastern subtropical dominant, and western subtropical dominant jet superposition events. The first column lists the category of QGPV, and the second column identifies the jet superposition event type. The third column identifies the spatial domain used to isolate each category of QGPV as a function of event type. For polar cyclonic and tropical anticyclonic QGPV anomalies, the spatial domain for each event type is referenced in the text as the "near-jet environment." The fourth column lists the criteria used to partition the QGPV within the specified spatial domain, and the fifth column identifies the lateral and horizontal boundary conditions used to invert each category of QGPV for its associated geopotential. The reader is referred to section 3a for explanations of the variables included within the table.

QGPV classification				
Category of QGPV	Event type	Spatial domain	Criteria	Boundary condition
Polar cyclonic QGPV anomalies (q_{cyc})	Polar	20°–50°N 120°–85°W	$q' \geq 4 \times 10^{-5}\,s^{-1}$ in the 700–150-hPa layer	$\phi_i' = 0$ on all lateral and horizontal boundaries
	East subtropical	25°–70°N 105°–55°W		
	West subtropical	30°–70°N 160°–100°W		
Tropical anticyclonic QGPV anomalies (q_{ant})	Polar	20°–30°N 112°–87°W	$q' \leq -4 \times 10^{-5}\,s^{-1}$ in the 700–150-hPa layer	$\phi_i' = 0$ on all lateral and horizontal boundaries
	East subtropical	25°–70°N 90°–30°W		
	West subtropical	20°–55°N 150°–90°W		
Residual QGPV anomalies (q_{res})	All event types	10°–80°N 150°E–10°W	All q' in the 700–50-hPa layer, excluding polar cyclonic and tropical anticyclonic QGPV anomalies	$\phi_i' = \phi - \phi_m$ on all lateral and horizontal boundaries at and above 700 hPa; $\phi_i' = 0$ below 700 hPa
Lower-tropospheric QGPV anomalies (q_{lt})	All event types	10°–80°N 150°E–10°W	All q' in the 1000–750-hPa layer	$\phi_i' = \phi - \phi_m$ on all lateral and horizontal boundaries below 700 hPa; $\phi_i' = 0$ at and above 700 hPa
Mean QGPV (q_m)	All event types	10°–80°N 150°E–10°W	q_m is calculated using the composite climatological mean geopotential based on all days that feature a superposition within a particular event type	ϕ_m on all lateral and horizontal boundaries

The perturbation QGPV q' for each event type is calculated as the difference between q and q_m, and is partitioned into four categories: 1) polar cyclonic QGPV anomalies, 2) tropical anticyclonic QGPV anomalies, 3) residual QGPV anomalies, and 4) lower-tropospheric QGPV anomalies. Polar cyclonic QGPV anomalies q_{cyc} are defined as QGPV anomalies in the near-jet environment (specified in the Table 1 caption) within the 700–150-hPa layer with a value $\geq 4 \times 10^{-5}\,s^{-1}$. Tropical anticyclonic QGPV anomalies q_{ant} are defined as QGPV anomalies in the near-jet environment within the 700–150-hPa layer with a value $\leq -4 \times 10^{-5}\,s^{-1}$. Residual QGPV anomalies q_{res} are defined as all QGPV anomalies in the 700–50-hPa layer, excluding q_{cyc} and q_{ant}. Physically, q_{res} describes the background upper-tropospheric flow pattern within which the polar and subtropical jets superpose, and includes the influence of circulations induced by upper-tropospheric ridges upstream and downstream of the jet superposition (e.g., Fig. 2a). Lower-tropospheric QGPV anomalies q_{lt} are defined as all QGPV anomalies within the 1000–750-hPa layer, and include the circulations induced by surface cyclones and anticyclones. A distribution of upper-tropospheric QGPV anomalies at the time of superposition for each event type, and an illustration of how those anomalies are partitioned into the categories described above, is shown in Figs. 5a–c. In particular, note that the juxtaposition of q_{cyc} and q_{ant} in Figs. 5a–c resembles the juxtaposition of PV anomalies within the conceptual model shown in Fig. 1a.

Each of the four categories of perturbation QGPV q_i' are inverted using successive overrelaxation using a relaxation factor of 1.8 to determine the perturbation geopotential ϕ_i' attributed to each category of QGPV based on the relationship:

$$q_i' = \frac{1}{f_o}\nabla^2\phi_i' + f_o\frac{\partial}{\partial p}\left(\frac{1}{\sigma_r}\frac{\partial\phi_i'}{\partial p}\right). \quad (3)$$

Motivated by the discussion in Hakim et al. (1996, 2182–2187), we adopt homogeneous Dirichlet boundary conditions

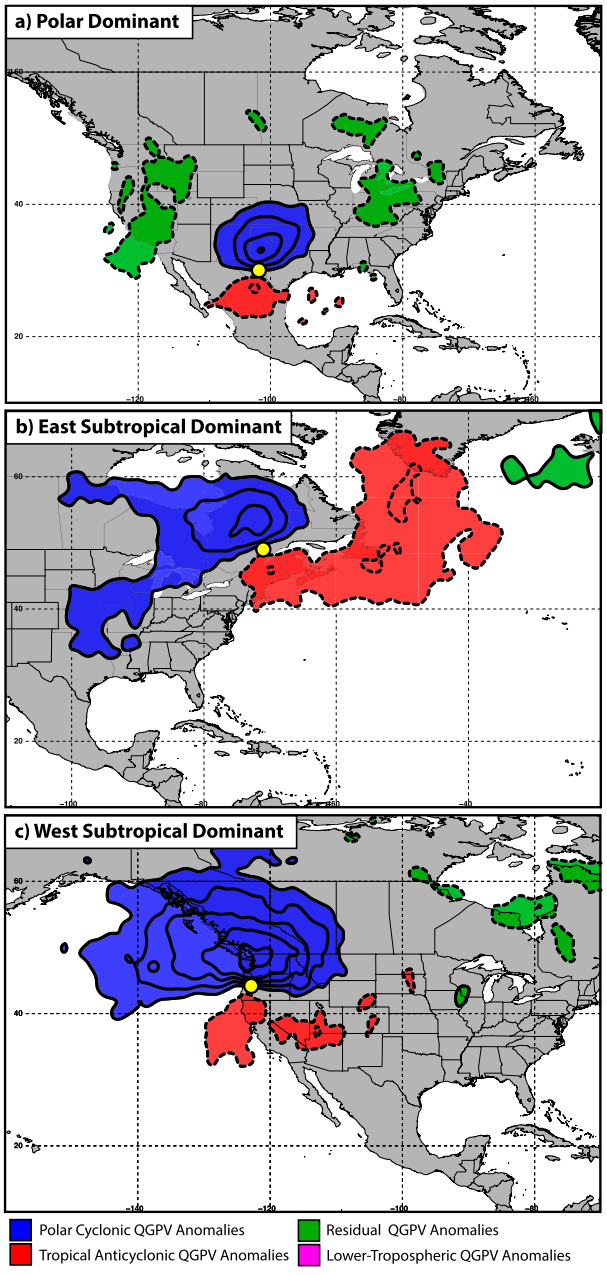

FIG. 5. 250-hPa QGPV anomalies (black lines every $4 \times 10^{-5}\,s^{-1}$, solid when positive and dashed when negative) at the time of superposition for polar dominant jet superposition events. The plotted QGPV anomalies are shaded to illustrate the QGPV classification scheme outlined in Table 1 and described in the text. (b) As in (a), but for 300-hPa QGPV anomalies at the time of superposition for eastern subtropical dominant events. (c) As in (a), but for 300-hPa QGPV anomalies at the time of superposition for western subtropical dominant events.

when inverting (3) for each category of the perturbation QGPV within the same domain used to construct the event composites. The boundary conditions used to invert each category of the perturbation QGPV distribution are listed in the rightmost column of Table 1. The boundary conditions and linear differential operator in (1), (2), and (3) ensure that $\phi = \phi_m + \sum_{i=1}^{n} \phi_i'$.

Under adiabatic and frictionless conditions, the **Q** vector is defined as the temporal rate of change of the horizontal temperature gradient following the geostrophic wind (e.g., Hoskins et al. 1978; Hoskins and Pedder 1980). To determine the vertical-motion pattern associated with each category of QGPV during an event type, a distribution of **Q** vectors is calculated in association with each category of QGPV according to (4):

$$\mathbf{Q} = -\frac{R}{p}\left[\left(\frac{\partial \mathbf{V}_g}{\partial x}\cdot\nabla T\right),\left(\frac{\partial \mathbf{V}_g}{\partial y}\cdot\nabla T\right)\right]. \tag{4}$$

In (4), the geostrophic wind is defined as $\mathbf{V}_g = -(1/f_o)(\hat{k}\times\nabla\phi)$, R is the gas constant for dry air, T is the composite temperature field, and p is the pressure. Note that within the expression for the geostrophic wind ϕ_m or ϕ_i' can be substituted for ϕ to calculate the geostrophic wind associated with each category of QGPV, such that $\mathbf{V}_g = \mathbf{V}_{gm} + \sum_{i=1}^{n} \mathbf{V}_{gi}'$. At this juncture, the composite temperature field is not partitioned in the calculation of **Q** vectors associated with each category of QGPV, but will be partitioned in section 3c.

The divergence of **Q** associated with each category of QGPV is substituted independently into the right-hand side of the QG–ω equation (5) to calculate the QG vertical motion associated with each category of QGPV:

$$\sigma_r\nabla^2\omega_a + f_o^2\frac{\partial^2\omega_a}{\partial p^2} = -2\nabla\cdot\mathbf{Q}, \tag{5}$$

where the full adiabatic contribution to the QG vertical motion ω_a is equal to the sum of the vertical motion associated with the mean QGPV and each category of perturbation QGPV, such that $\omega_a = \omega_m + \sum_{i=1}^{n}\omega_i'$. An inversion of (5) for each category of QGPV is performed using successive overrelaxation with a relaxation factor of 1.8 in the same domain used to construct the event composites. In all inversions of (5), ω_a is set to 0 on the lateral and horizontal boundaries of the domain. A physical interpretation of (4) and (5) reveals that the QG vertical motion that corresponds to a particular category of QGPV is associated with changes in the orientation and magnitude of the composite horizontal temperature gradient that are effected by the geostrophic wind induced by that particular category of QGPV.

Based on the established influence of diabatic heating on the development of jet superposition events (e.g., Winters and Martin 2016, 2017; Winters et al. 2020), the diabatic contribution to the QG vertical motion ω_d is determined via the version of the QG–ω equation shown below:

$$\sigma_r\nabla^2\omega_d + f_o^2\frac{\partial^2\omega_d}{\partial p^2} = -\frac{R}{c_p p}\nabla^2 J, \tag{6}$$

where the diabatic heating rate J is calculated using the composite 3-h average diabatic temperature tendency output from the CFSR during a particular event type. An inversion of (6) for ω_d is performed in the same manner as (5), and the sum of

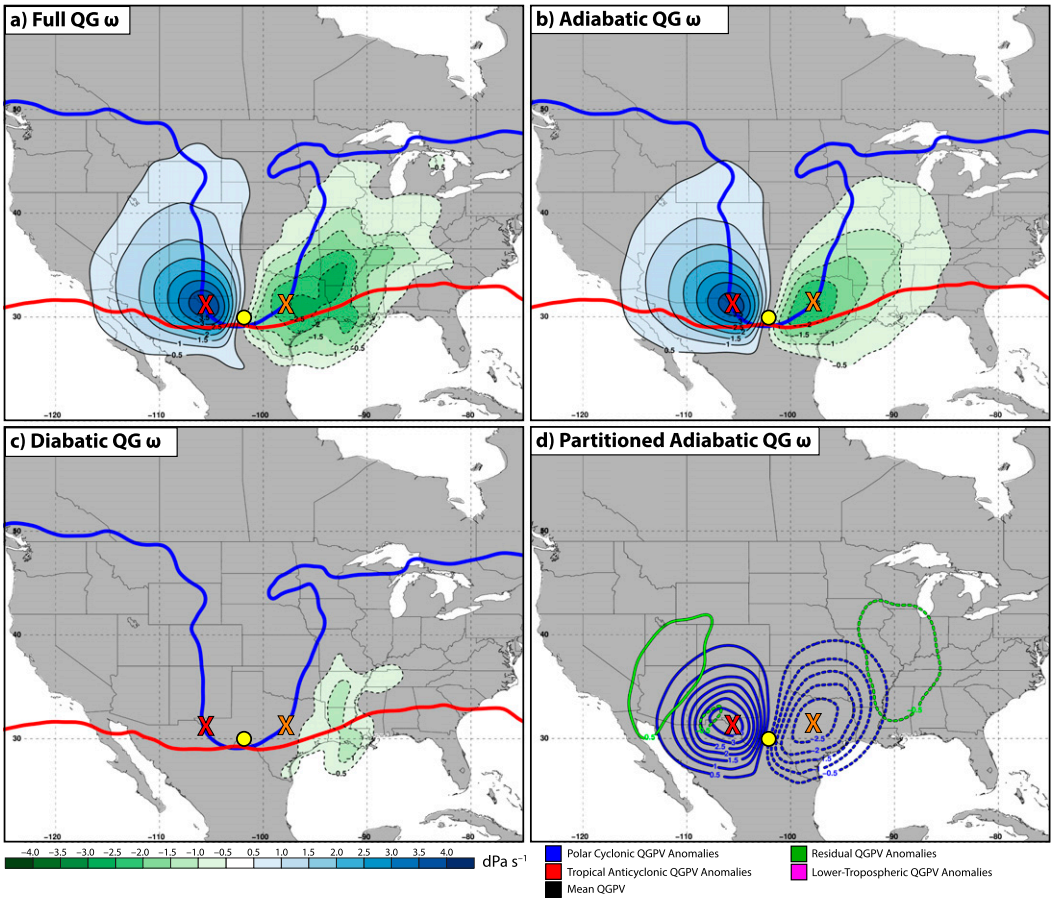

FIG. 6. (a) 500-hPa QG ω is shaded according to the legend (dPa s^{-1}), and the positions of the 2-PVU contour within the 320–325-K layer and 345–350-K layer at the time of a polar dominant jet superposition are indicated by the thick blue line and thick red line, respectively. (b) As in (a), but for the adiabatic contribution to the full QG vertical motion ω_a. (c) As in (a), but for the diabatic contribution to the full QG vertical motion ω_d. (d) The QG ω associated with each category of QGPV. Lines are plotted every 0.5 dPa s^{-1}, are solid when positive and dashed when negative, and are colored according to the categories of QGPV listed in the legend. In all panels, the yellow dot indicates the average location of jet superposition, and the red "X" and orange "X" denote the locations of maximum ω_a descent and ω_a ascent, respectively.

the adiabatic and diabatic contributions to the QG vertical motion returns the full QG vertical motion ω, such that $\omega = \omega_a + \omega_d$.

b. *Vertical motion associated with each category of QGPV*

The 500-hPa QG ω patterns at the time of jet superposition for polar dominant, eastern subtropical dominant, and western subtropical dominant events are shown in Figs. 6a, 7a, and 8a, respectively, and are qualitatively similar to the composite vertical-motion patterns associated with each event type (Figs. 2a,c,e). Figures 6a–c reveal that the contribution from ω_a to the 500-hPa QG ω pattern during polar dominant events is larger than ω_d. Therefore, adiabatic processes account for a majority of the 500-hPa QG ω pattern observed during polar dominant events. Figures 6b and 6d further reveal that the largest fraction of the 500-hPa QG ω_a pattern is attributed to the geostrophic wind induced by polar cyclonic QGPV anomalies $\mathbf{V}_{cyc}$. A minor contribution to the 500-hPa QG ω_a pattern upstream and downstream of polar dominant jet superpositions is associated with the geostrophic wind induced by residual QGPV anomalies $\mathbf{V}_{res}$. This minor contribution from $\mathbf{V}_{res}$ highlights the influence of upper-tropospheric ridges upstream and downstream of the jet superposition (Fig. 2a) on the development of QG vertical motion within the near-jet environment.

The 500-hPa QG ω pattern during eastern subtropical dominant events (Fig. 7a) implies that QG descent upstream of the jet superposition is predominantly associated with ω_a (Figs. 7a–c), and that the largest fraction of ω_a descent is attributed to $\mathbf{V}_{cyc}$ (Figs. 7b,d). Additional contributions to ω_a descent in the vicinity of eastern subtropical dominant events are associated with $\mathbf{V}_{res}$ and the geostrophic wind induced by lower-tropospheric QGPV anomalies $\mathbf{V}_{lt}$ (Figs. 7b,d). Downstream of the jet superposition, the geostrophic wind induced by each

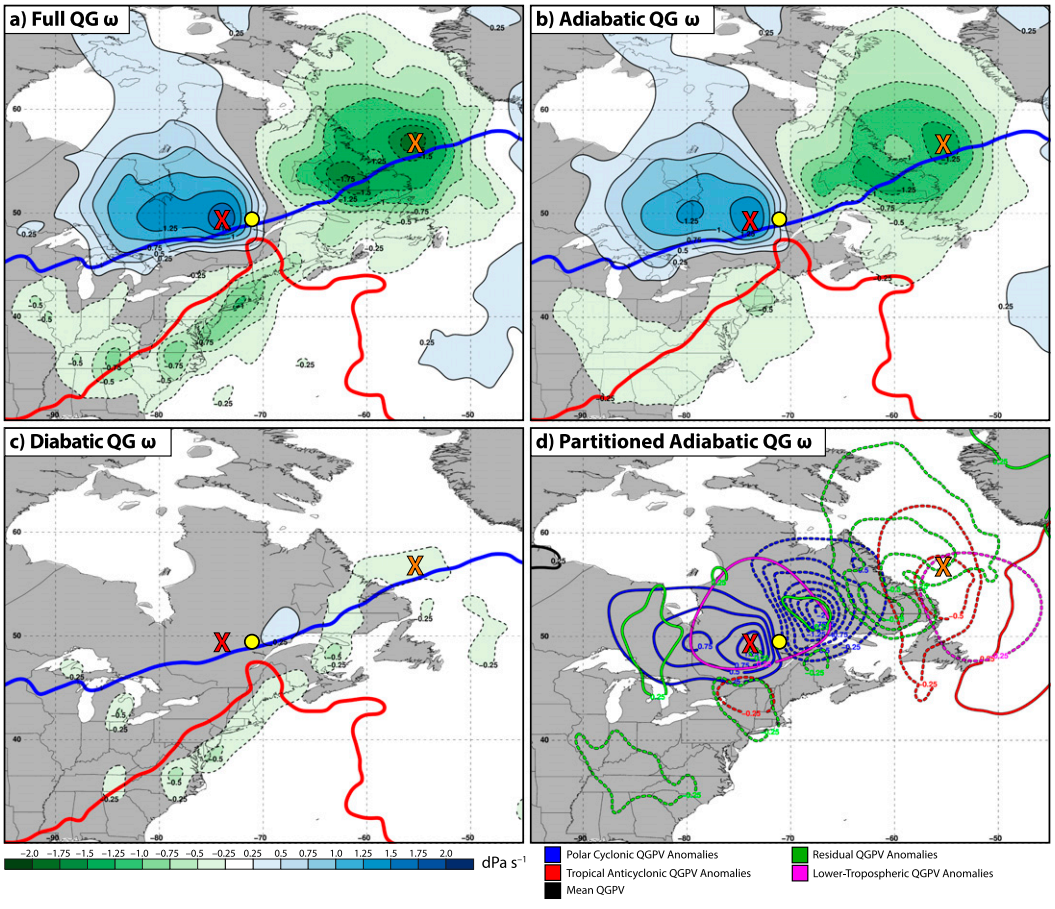

FIG. 7. As in Fig. 6, but at the time of an eastern subtropical dominant jet superposition. QG ω is shaded and contoured every 0.25 dPa s^{-1}.

category of perturbation QGPV contributes to varying degrees to a broad area of ω_a ascent over southeastern Canada, with the largest contribution to ω_a ascent immediately downstream of the jet superposition associated with $\mathbf{V}_{\text{cyc}}$ (Figs. 7b,d). As for polar dominant events, ω_a accounts for a larger fraction of QG ascent during eastern subtropical dominant events compared to ω_d (Figs. 7a–c). The distribution of ω_d is nonnegligible, however, and is characterized by a linear band of ascent that extends along the east coast of North America on the equatorward side of the jet (Fig. 7c).

The 500-hPa QG ω pattern during western subtropical dominant events (Figs. 8a–c) is dominated by ω_a, with the largest fraction of the ω_a pattern associated with $\mathbf{V}_{\text{cyc}}$ (Figs. 8b,d). Therefore, polar cyclonic QGPV anomalies are associated with a large majority of the 500-hPa QG ω patterns diagnosed in the vicinity of every jet superposition event type. This observation implies that the QG vertical motion induced by $\mathbf{V}_{\text{cyc}}$ is dominant in vertically restructuring the tropopause in the vicinity of jet superpositions compared to the vertical motion associated with all other categories of QGPV. As observed during eastern subtropical dominant events, a minor contribution to ω_a descent during western subtropical dominant events is associated with $\mathbf{V}_{\text{lt}}$ (Figs. 7d, 8d). The vertical motion associated with lower-tropospheric QGPV anomalies during eastern and western subtropical dominant events is indicative of the potential for the tropospheric-deep circulations induced by surface cyclones (refer to Winters et al. 2020; their Figs. 8i and 11i) to have a relatively stronger influence in vertically restructuring the tropopause during eastern and western subtropical dominant events compared to polar dominant events. QG ascent far downstream of western subtropical dominant jet superpositions is associated with $\mathbf{V}_{\text{res}}$ (Fig. 8d), which highlights the impact of a downstream upper-tropospheric ridge (Fig. 2e) on forcing QG ascent during this event type.

Notably, the geostrophic wind induced by tropical anticyclonic QGPV anomalies $\mathbf{V}_{\text{ant}}$ is not associated with a substantial contribution to the ω_a pattern during western subtropical dominant events (Fig. 8d), whereas $\mathbf{V}_{\text{ant}}$ is associated with a more substantial contribution to the ω_a pattern during eastern subtropical dominant events (Fig. 7d). The larger contribution to the ω_a pattern from $\mathbf{V}_{\text{ant}}$ during eastern subtropical dominant events is partly attributed to the stronger anticyclonic curvature of the perturbation upper-tropospheric ridge that characterizes eastern subtropical dominant compared to western subtropical dominant events (cf. Figs. 2c,e). This stronger anticyclonic curvature subsequently contributes to

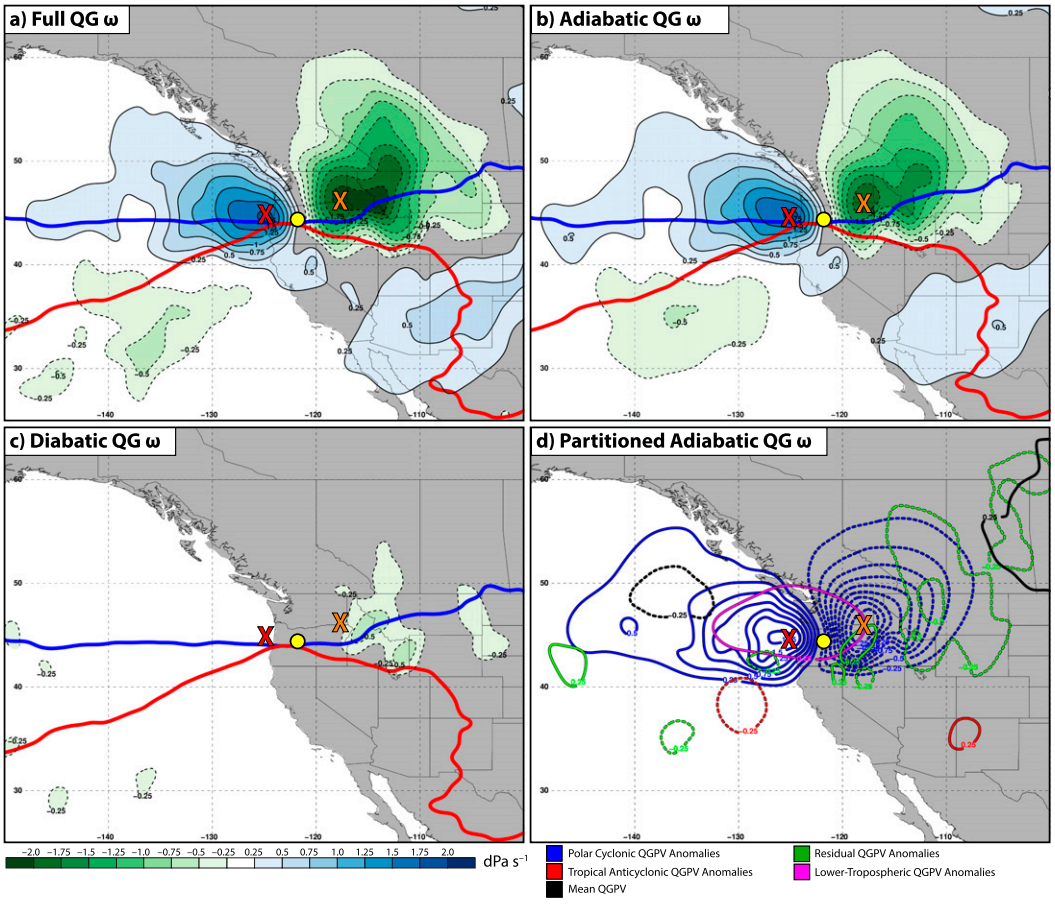

FIG. 8. As in Fig. 7, but at the time of a western subtropical dominant jet superposition.

the zonally oriented couplet of ascent and descent associated with $\mathbf{V}_{\text{ant}}$ that is centered near 50°W during eastern subtropical dominant events (Fig. 7d). The stronger perturbation upper-tropospheric ridge during eastern compared to western subtropical dominant events also reflects the more pronounced effects of diabatic heating during eastern subtropical dominant events given the proximity of those events to the warm sea surface temperatures of the Gulf Stream (not shown).

c. *Vertical motion associated with interactions between categories of QGPV*

The perturbation geopotential ϕ_i' that characterizes each category of perturbation QGPV is associated with a perturbation temperature T_i' that can be determined via the hydrostatic relationship ($\partial\phi_i'/\partial p = -RT_i'/p$), such that $T = T_r + T_m + \sum_{i=1}^{n} T_i'$. In the latter equation, T_r represents the reference temperature on an isobaric surface and T_m represents the composite climatological mean temperature on those calendar days that feature a jet superposition for a particular event type after the reference temperature has been removed. The geostrophic wind and temperature associated with each category of QGPV can be substituted into (4) in a variety of combinations to calculate distributions of $\mathbf{Q}$ vectors that result from interactions between the geostrophic wind induced by a particular category of QGPV and the baroclinicity associated with another category of QGPV. Therefore, the forthcoming analysis of interaction terms expands upon the results presented in section 3b by providing a measure of the degree to which interactions between QGPV anomalies contribute to the development QG vertical motion within the near-jet environment.

The aforementioned partition of the geopotential and temperature fields results in a total of 25 possible interaction terms. Namely, there are five geostrophic wind fields that correspond to the mean QGPV and the four categories of perturbation QGPV (e.g., the rows in Figs. 10 and 11), and these five geostrophic wind fields can interact with five temperature fields that correspond to the mean QGPV and the four categories of perturbation QGPV (e.g., the columns in Figs. 10 and 11). The divergence of $\mathbf{Q}$ associated with each interaction term can be substituted into the right-hand side of (5) and inverted to determine the QG vertical motion associated with each interaction term, such that the QG vertical motion associated with all 25 interaction terms sum to ω_a during a particular event type (e.g., Figs. 6b, 7b, 8b). The QG vertical motion associated with interactions between the geostrophic wind induced by a single category of QGPV (e.g., $\mathbf{V}_{\text{cyc}}$) and all five temperature fields during a particular event type sum to the QG vertical motion

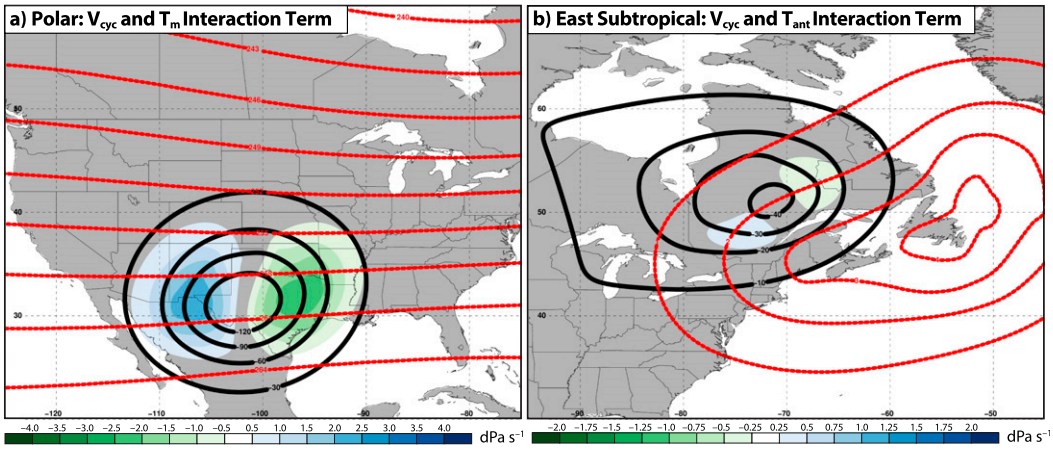

FIG. 9. (a) 500-hPa QG ω associated with the interaction between $\mathbf{V}_{\text{cyc}}$ and T_m is shaded according to the legend (dPa s^{-1}), the 500-hPa perturbation geopotential height associated with polar cyclonic QGPV anomalies is contoured in black every −30 m, and the climatological mean temperature field at 500 hPa is contoured in dashed red every 3 K at the time of a polar dominant jet superposition. (b) 500-hPa QG ω associated with the interaction between $\mathbf{V}_{\text{cyc}}$ and T_{ant} is shaded according to the legend (dPa s^{-1}), the 500-hPa perturbation geopotential height associated with polar cyclonic QGPV anomalies is contoured in black every −10 m, and the 500-hPa perturbation temperature field associated with tropical anticyclonic QGPV anomalies is contoured in dashed red every +1 K at the time of an eastern subtropical dominant jet superposition.

associated with that geostrophic wind field in Figs. 6d, 7d, or 8d (e.g., the blue contours in Figs. 6d, 7d, or 8d for polar cyclonic QGPV anomalies).

Physically, the QG vertical motion attributed to each interaction term corresponds to changes in the orientation and magnitude of the horizontal temperature gradient associated with a particular category of QGPV that are effected by the geostrophic wind induced by another category of QGPV. For example, the QG vertical motion attributed to the interaction between $\mathbf{V}_{\text{cyc}}$ and T_m during polar dominant events corresponds to changes in the orientation and magnitude of the mean temperature gradient that are accomplished by the geostrophic wind induced by polar cyclonic QGPV anomalies (e.g., Fig. 9a). Similarly, an interaction between $\mathbf{V}_{\text{cyc}}$ and T_{ant} during eastern subtropical dominant events corresponds to changes in the orientation and magnitude of the perturbation temperature gradient attributed to tropical anticyclonic QGPV anomalies that are accomplished by the geostrophic wind induced by polar cyclonic QGPV anomalies (e.g., Fig. 9b). In both examples shown in Fig. 9, it can be inferred that $\mathbf{V}_{\text{cyc}}$ facilitates a local maximum in geostrophic warm-air advection in areas of QG ascent, and a local maximum in geostrophic cold-air advection in areas of QG descent, which provides further context for the development of QG vertical motion associated with each interaction term.

Figure 10 shows the percentage of 500-hPa ω_a descent associated with all 25 interaction terms at the location of maximum ω_a descent (red X marks in Figs. 6–8) during polar dominant, eastern subtropical dominant, and western subtropical dominant events. All percentages shown in Fig. 10 are calculated by dividing the 500-hPa QG vertical motion associated with a particular interaction term by ω_a at the location of the red X in its corresponding event type (i.e., Figs. 6b, 7b, 8b). This fraction is then multiplied by 100 to determine the percentage of ω_a associated with that particular interaction term. Consistent with the results discussed in Figs. 6–8, Fig. 10 indicates that the largest fraction of ω_a descent is associated with $\mathbf{V}_{\text{cyc}}$ for all event types. More specifically, Fig. 10 reveals that the interactions between $\mathbf{V}_{\text{cyc}}$ and T_m, and $\mathbf{V}_{\text{cyc}}$ and T_{cyc}, dominate the production of ω_a descent across all event types.

The ω_a descent pattern during eastern and western subtropical dominant events also features a substantial contribution from the interaction between $\mathbf{V}_{\text{cyc}}$ and T_{ant}. The relative importance of this interaction term during subtropical dominant events is due to the larger magnitude of tropical anticyclonic QGPV anomalies during both subtropical dominant event types compared to polar dominant events (i.e., note that the magnitude of geopotential height anomalies on the equatorward side of the superposed jet in Figs. 2a, 2c, and 2e is larger for both types of subtropical dominant events compared to polar dominant events). Consequently, tropical anticyclonic QGPV anomalies contribute more substantially during subtropical dominant events compared to polar dominant events to the structure of the composite horizontal temperature gradient. Figure 10 also identifies a nonnegligible contribution to ω_a descent across all event types from the interaction between $\mathbf{V}_{\text{lt}}$ and T_m. This result highlights the influence of surface cyclones (refer to Winters et al. 2020; their Figs. 5i, 8i, and 11i) on the structure of the mean upper-tropospheric flow pattern (e.g., Hoskins et al. 1985, 928–930; Davis and Emanuel 1991; Davis 1992a; Nielsen-Gammon and Lefevre 1996; Winters and Martin 2017).

The fraction of 500-hPa ω_a ascent attributed to each interaction term at the location of maximum ω_a ascent (orange X marks in Figs. 6b, 7b, and 8b) is shown in Fig. 11 for each event type. During polar dominant events, the largest fraction of ω_a

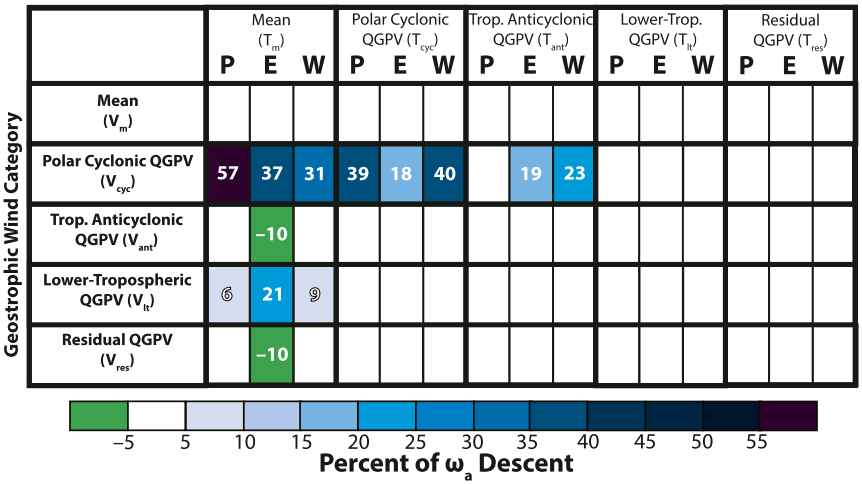

FIG. 10. The percent of the total ω_a descent (shaded according to the legend) that is associated with interactions between the geostrophic winds induced by each category of QGPV anomalies (rows), and the temperature fields associated with each category of QGPV anomalies (columns). The intersection of a row and column represents a particular interaction term, with the three boxes within an interaction term indicating the percent of ω_a descent that is associated with that interaction term at the location of maximum ω_a descent (red "X" marks in Figs. 6–8) during polar dominant (P), eastern subtropical dominant (E), and western subtropical dominant (W) jet superposition events. The numeric percentage of ω_a descent associated with each interaction term is listed for those boxes in which the absolute value of the percent of ω_a descent is greater than 5%. Negative percentages correspond to interaction terms that are associated with QG ascent at the location of maximum ω_a descent.

ascent downstream of the jet superposition is associated with interactions between $\mathbf{V}_{cyc}$ and T_m, and $\mathbf{V}_{cyc}$ and T_{cyc}. This result is analogous to that found for ω_a descent during polar dominant events (Fig. 10), and solidifies the observation that the QG vertical-motion pattern during polar dominant events is predominantly fostered by the presence of a strong polar cyclonic QGPV anomaly on the poleward side of the jet and its attendant baroclinicity.

The location of maximum ω_a ascent during eastern subtropical dominant events is displaced farther downstream of the location of jet superposition compared to polar dominant events (cf. Fig. 7b with Fig. 6b). Consequently, the contribution to ω_a ascent from $\mathbf{V}_{cyc}$ is minimal at this location for eastern subtropical dominant events (Fig. 11). The selection of a grid point closer to the location of jet superposition during eastern subtropical dominant events, however, reveals that $\mathbf{V}_{cyc}$ dominates the production of ω_a ascent in the immediate vicinity of the jet superposition (not shown). Nevertheless, Fig. 11 demonstrates that in locations farther downstream of the jet superposition, the largest fraction of ω_a ascent is associated with the interactions between $\mathbf{V}_{ant}$ and T_m, $\mathbf{V}_{lt}$ and T_m, and $\mathbf{V}_{res}$ and T_m. The interactions between $\mathbf{V}_{ant}$ and T_m, and $\mathbf{V}_{res}$ and T_m highlight the combined influence of perturbation upper-tropospheric ridges within the near-jet environment, and their separate interactions with the mean temperature gradient, on the production of ω_a ascent. Similarly, the interaction between $\mathbf{V}_{lt}$ and T_m highlights the influence of a surface cyclone (refer to Winters et al. 2020; their Fig. 8i), and its interaction with the mean temperature gradient, on the production of ω_a ascent. Notably, the interactions between $\mathbf{V}_{ant}$ and T_{ant}, and $\mathbf{V}_{res}$ and T_{ant}, also contribute a nonnegligible amount to QG vertical motion at the location of maximum ω_a ascent. This result reveals an important contribution to the production of ω_a ascent during eastern subtropical dominant events that results from the interactions between perturbation upper-tropospheric ridges within the near-jet environment and the baroclinicity attributed to tropical anticyclonic QGPV anomalies (Fig. 11).

As observed during polar dominant events, western subtropical dominant events feature large contributions to 500-hPa ω_a ascent from $\mathbf{V}_{cyc}$ (Fig. 11), given that the location of maximum ω_a ascent resides in close proximity to the jet superposition (Fig. 8b). In particular, Fig. 11 shows substantial contributions to ω_a ascent from $\mathbf{V}_{cyc}$ and its separate interactions with T_m, T_{cyc}, and T_{ant}. This result reveals that the total tropospheric baroclinicity in the vicinity of western subtropical dominant jet superpositions results from the presence of both strong polar cyclonic and tropical anticyclonic QGPV anomalies in the near-jet environment, with a minor contribution from the mean temperature field. Nevertheless, $\mathbf{V}_{cyc}$ is the primary circulation that interacts with the strong baroclinicity assembled in the vicinity of western subtropical dominant jet superpositions to produce ω_a ascent.

To summarize, the QG vertical-motion pattern during polar dominant events is predominantly attributed to the geostrophic wind induced by polar cyclonic QGPV anomalies and its interaction with the baroclinicity induced by polar cyclonic QGPV anomalies and the mean QGPV. The influence of polar cyclonic QGPV anomalies on the production of QG vertical

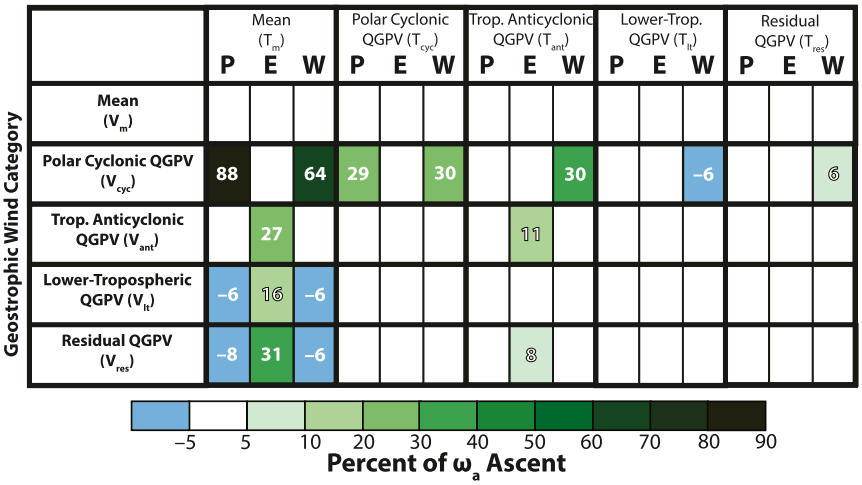

FIG. 11. As in Fig. 10, but for the percent of ω_a ascent (shaded according to the legend) that is associated with interactions between the geostrophic winds induced by each category of QGPV anomalies and the temperature fields associated with each category of QGPV anomalies at the location of maximum ω_a ascent (orange "X" marks in Figs. 6–8) during polar dominant (P), eastern subtropical dominant (E), and western subtropical dominant (W) jet superposition events. The numeric percentage of ω_a ascent associated with each interaction term is listed for those boxes in which the absolute value of the percent of ω_a ascent is greater than 5%. Negative percentages correspond to interaction terms that are associated with QG descent at the location of maximum ω_a ascent.

motion is also substantial during eastern and western subtropical dominant events, however, tropical anticyclonic QGPV anomalies, lower-tropospheric QGPV anomalies (i.e., surface cyclones), and residual QGPV anomalies (i.e., flanking upper-tropospheric ridges) make relatively larger contributions to the QG vertical-motion pattern via their induced geostrophic winds and/or via their contributions to the tropospheric baroclinicity during both types of subtropical dominant events compared to polar dominant events. Consequently, the QG vertical-motion patterns during both types of subtropical dominant events are more complex than those observed during polar dominant events, and are dependent on the nuanced configuration of upper- and lower-tropospheric QGPV anomalies that reside within the near-jet environment.

4. Along- and across-isotherm vertical motion in the vicinity of jet superpositions

The character of QG vertical motion in the vicinity of jet superpositions can be further evaluated by partitioning the **Q** vector into an along-isotherm $\mathbf{Q}_s$ and an across-isotherm $\mathbf{Q}_n$ component. This partition of **Q** is performed within a left-hand coordinate system[2] following Martin (1999, 2006, 2014) in which the unit vector **s** is aligned in the along-isotherm direction $[(\hat{\mathbf{k}} \times \nabla T)/|\nabla T|]$, and the unit vector **n** is directed 90° clockwise of **s** and points toward warmer air $(\nabla T/|\nabla T|)$. The along-isotherm and across-isotherm components of **Q** are defined in this coordinate system as follows:

$$\mathbf{Q}_s = \left[\frac{\mathbf{Q} \cdot (\hat{\mathbf{k}} \times \nabla T)}{|\nabla T|}\right] \frac{(\hat{\mathbf{k}} \times \nabla T)}{|\nabla T|}, \tag{7a}$$

$$\mathbf{Q}_n = \left(\frac{\mathbf{Q} \cdot \nabla T}{|\nabla T|}\right) \frac{\nabla T}{|\nabla T|}, \tag{7b}$$

where $\mathbf{Q} = \mathbf{Q}_s + \mathbf{Q}_n$. Equations (7a) and (7b) indicate that changes in the orientation of the horizontal temperature gradient following the geostrophic wind are diagnosed by $\mathbf{Q}_s$, whereas changes in the magnitude of the horizontal temperature gradient following the geostrophic wind are diagnosed by $\mathbf{Q}_n$ (e.g., Keyser et al. 1988, 1992; Martin 2006, their Fig. 2).

The divergence of $\mathbf{Q}_s$ and $\mathbf{Q}_n$ can be separately substituted into the right-hand side of (5) to calculate the along-isotherm component of the vertical motion ω_s and the across-isotherm component of the vertical motion ω_n, such that $\omega_a = \omega_s + \omega_n$. As previously discussed, ω_s corresponds to the vertical motion associated with synoptic-scale waves, while ω_n corresponds to the vertical motion associated with frontal circulations in the vicinity of the jet. Therefore, this partition of the **Q** vector provides insight into the extent to which QG vertical motions within the near-jet environment are associated with an amplified upper-tropospheric flow pattern (i.e., ω_s) or frontal circulations that result from the formation of strong baroclinicity in the vicinity of the superposed jet (i.e., ω_n).

[2] Note that these conventions differ from those utilized by Keyser et al. (1992), who partition **Q** using a right-hand coordinate system. These different conventions do not alter the physical interpretation of the along-isotherm and across-isotherm components of **Q**.

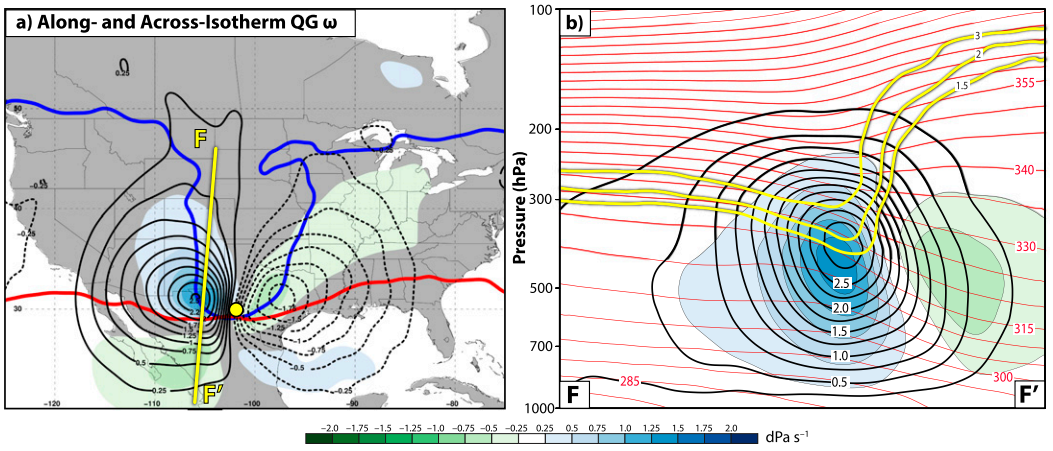

FIG. 12. (a) 500-hPa ω_n is shaded according to the legend (dPa s^{-1}), 500-hPa ω_s is contoured in black every 0.25 dPa s^{-1}, solid when positive and dashed when negative, and the positions of the 2-PVU contour within the 320–325-K layer and 345–350-K layer at the time of a polar dominant jet superposition are indicated by the thick blue line and thick red line, respectively. The yellow dot indicates the average location of jet superposition. (b) Cross section along F–F′, as indicated in (a), with potential temperature (red lines every 5 K), the 1.5-, 2-, and 3-PVU contours (thick yellow lines), ω_n (shaded according to the legend; dPa s^{-1}), and ω_s (black contours every 0.25 above 0.25 dPa s^{-1}).

The ω_s and ω_n patterns associated with polar dominant events are shown in Fig. 12a. The ω_s pattern features a dipole centered on the location of jet superposition, with QG ascent situated downstream of the jet superposition and QG descent situated upstream. This dipole is consistent with the presence of an amplified upper-tropospheric trough on the poleward side of the jet (Fig. 2a; e.g., Sanders and Hoskins 1990, their Fig. 4). The ω_n pattern exhibits a quadrupole structure, with a thermally direct circulation beneath the confluent jet-entrance region and a thermally indirect circulation beneath the diffluent jet-exit region (Figs. 12a, 2a). This quadrupole structure is consistent with the idealized QG vertical-motion patterns anticipated in the vicinity of jets (e.g., Uccellini and Kocin 1987, their Fig. 3; Sanders and Hoskins 1990, their Figs. 5 and 6).

Consideration of the ω_s and ω_n patterns during polar dominant events indicates that ω_s is larger in magnitude than ω_n (Fig. 12a). Nevertheless, both ω_s and ω_n contribute to QG descent upstream of the jet superposition and QG ascent downstream of the jet superposition (Fig. 12a). A cross section upstream of the jet superposition confirms that ω_s contributes a larger amount to QG descent beneath and on the poleward side of the tropopause height minimum compared to ω_n (Fig. 12b). The ω_s and ω_n descent maxima are both located in close proximity to the tropopause height minimum, however, which suggests that ω_s and ω_n act together to facilitate the downward advection of high-PV air in the vicinity of the tropopause height minimum at this time (Fig. 2b). This downward advection of high-PV air subsequently contributes to the development of the steep, single-step tropopause structure observed at the time of jet superposition.[3]

The ω_s pattern during eastern subtropical dominant events features a dipole, with QG descent upstream of the jet superposition and QG ascent downstream of the jet superposition (Fig. 13a). The ω_n pattern exhibits a tripole structure, with a thermally direct circulation beneath the jet-entrance region and a weak area of ascent beneath the jet-exit region (Figs. 13a, 2c). A comparison between ω_s and ω_n demonstrates that ω_s descent is larger in magnitude than ω_n descent immediately upstream of the jet superposition, but is of the same magnitude as ω_n in locations farther upstream along the polar jet waveguide. As with polar dominant events, both ω_s and ω_n contribute to QG descent beneath and on the poleward side of the tropopause height minimum within the cross section shown in Fig. 13b. Notably, the ω_n descent maximum is not focused in close proximity to the tropopause height minimum, as it was during polar dominant events (cf. Figs. 13b, 12b). The maximum in ω_s descent is focused in close proximity to the tropopause height minimum, however, which suggests that ω_s descent dominates the production of downward PV advection and the formation of a steep, single-step tropopause structure within the cross section shown in Fig. 13b.

Similar to the other two jet superposition event types, the ω_s pattern during western subtropical dominant events features a dipole with QG descent upstream of the jet superposition and QG ascent downstream of the superposition (Fig. 14a). The ω_n pattern exhibits a quadrupole structure with a thermally direct circulation beneath the jet-entrance region and a thermally indirect circulation beneath the jet-exit region (Figs. 14a, 2e). Consistent with polar and eastern subtropical dominant events, the magnitude of ω_s is larger than ω_n in the immediate vicinity of western subtropical dominant events (Fig. 14a) and the cross section shown in Fig. 14b confirms that ω_s descent is larger in magnitude than

[3] Similar vertical-motion patterns to those shown in Figs. 12–14 are also obtained 12 h prior to jet superposition.

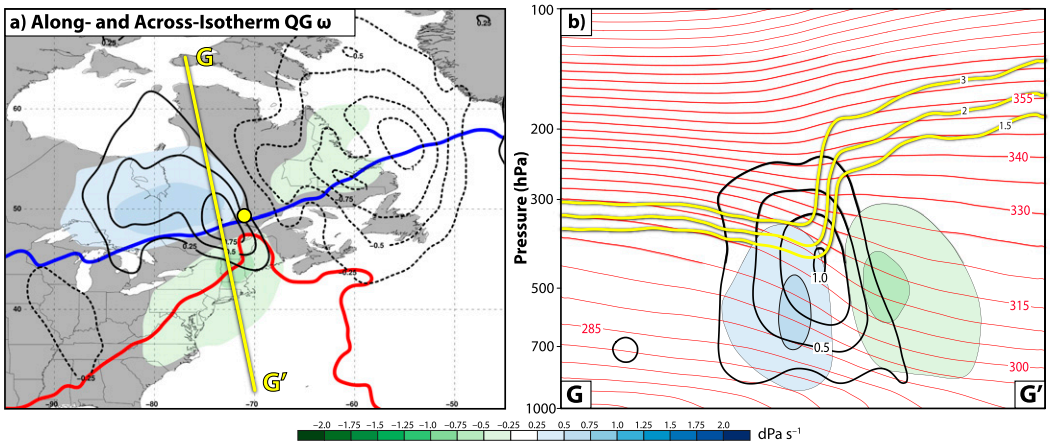

FIG. 13. (a) As in Fig. 12a, but for an eastern subtropical dominant jet superposition. (b) As in Fig. 12b, but for the cross section along G–G′, as indicated in (a).

ω_n descent beneath and on the poleward side of the tropopause height minimum. The ω_s and ω_n descent maxima are both focused in close proximity to the tropopause height minimum, similar to polar dominant events, which suggests that both ω_s and ω_n contribute to the development of the steep, single-step tropopause structure observed during western subtropical dominant events.

The contributions of ω_s and ω_n to ω_a in the vicinity of jet superpositions is further evaluated in Fig. 15. The right-hand side of each panel in Fig. 15 depicts the area-averaged ω_a ascent as a function of pressure across all grid points downstream of each jet superposition event type with $\omega_a < -0.5\,\text{dPa s}^{-1}$. The left-hand side of each panel in Fig. 15 depicts the area-averaged ω_a descent across all grid points upstream of each jet superposition event type with $\omega_a > 0.5\,\text{dPa s}^{-1}$. The area-averaged ω_a on a particular isobaric surface is also partitioned into its contributions from the area-averaged ω_s and ω_n, which are calculated by averaging ω_s and ω_n over the same area on an isobaric surface used to compute the area-averaged ω_a.

The area-averaged ω_s is considerably larger in magnitude than ω_n on all isobaric surfaces for polar dominant events (Fig. 15a). The dominance of ω_s during polar dominant events is associated with the presence of an amplified upper-tropospheric trough on the poleward side of the jet (Fig. 2a). The area-averaged ω_s also dominates ω_n during western subtropical dominant events (Fig. 15c), but not to the same degree as during polar dominant events (Fig. 15a). As with polar dominant events, the dominance of ω_s during western subtropical dominant events is associated with the presence of an upper-tropospheric trough on the poleward side of the jet (Fig. 2c). Nevertheless, the upper-tropospheric flow pattern during western subtropical dominant events is not as amplified compared to polar dominant events, which may explain the reduced dominance of the area-averaged ω_s relative to ω_n during western subtropical dominant events.

Whereas the area-averaged ω_s ascent dominates ω_n ascent during eastern subtropical dominant events, the area-averaged ω_s descent is of the same magnitude as ω_n descent below

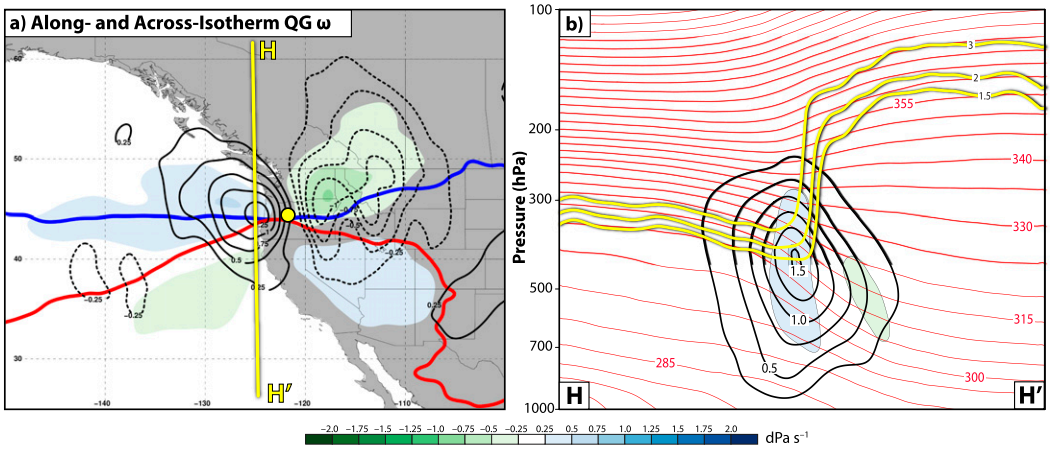

FIG. 14. (a) As in Fig. 12a, but for a western subtropical dominant jet superposition. (b) As in Fig. 12b, but for the cross section along H–H′, as indicated in (a).

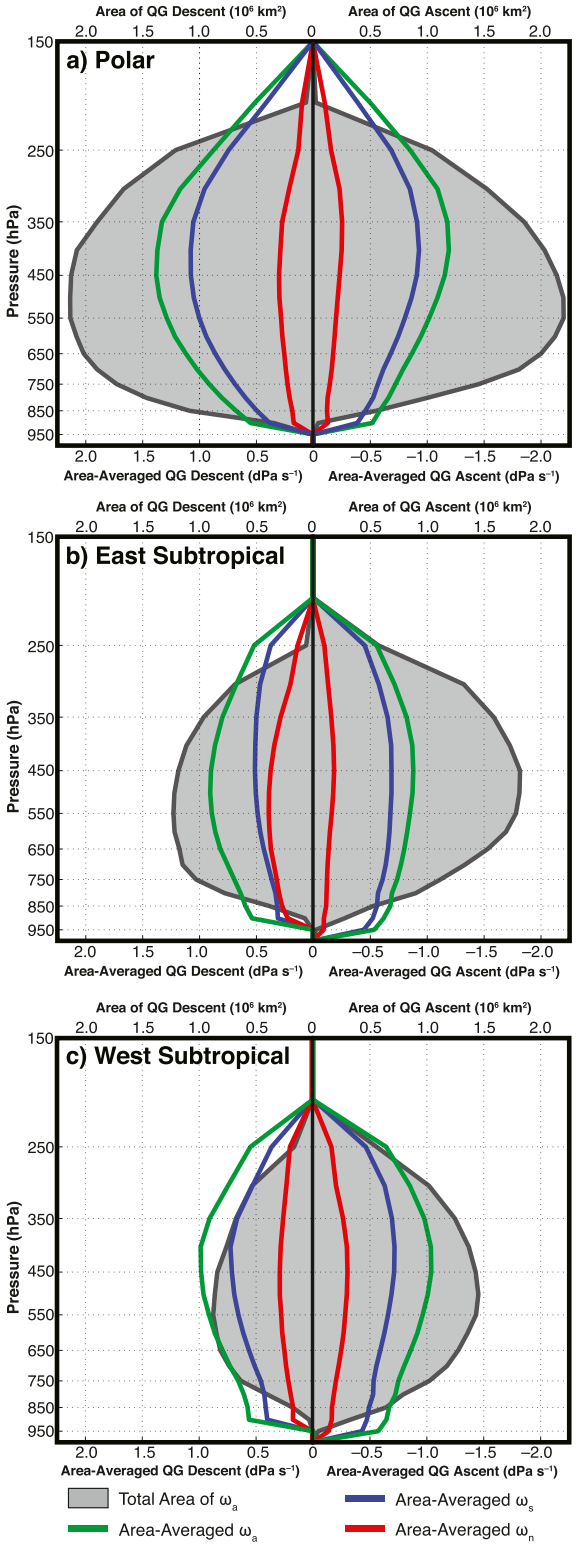

FIG. 15. (a) The area-averaged ω_a ascent downstream of polar dominant jet superpositions at locations in which $\omega_a < -0.5$ dPa s^{-1} (e.g., green shading in Fig. 6b) is shown as a function of pressure in green on the right-hand side of the plot. The area-averaged ω_a descent upstream of polar dominant jet superpositions at locations

500 hPa (Fig. 15b). The larger contribution from ω_n descent during eastern subtropical dominant events compared to polar dominant and western subtropical dominant events may be attributed to two factors. First, the upper-tropospheric flow pattern is more amplified downstream of eastern subtropical dominant events (Fig. 2c), whereas the strongest flow amplification occurs in the immediate vicinity of polar and western subtropical dominant events (Figs. 2a,e). The reduced flow amplification in the immediate vicinity of eastern subtropical dominant events subsequently reduces the contribution from the area-averaged ω_s descent to the area-averaged ω_a descent (Fig. 15b). Second, eastern subtropical dominant events often form along the east coast of North America (Winters et al. 2020; their Fig. 4c). Consequently, eastern subtropical dominant events feature stronger tropospheric baroclinicity than polar dominant and western subtropical dominant events due to the juxtaposition of a cold continental air mass and a warm subtropical air mass beneath the jet superposition (cf. the baroclinicity in Fig. 2d with Figs. 2b,f). The development of stronger baroclinicity during eastern subtropical dominant events results in a vigorous across-front ageostrophic circulation and a comparatively larger contribution to QG descent from ω_n beneath the jet-entrance region of eastern subtropical dominant events.

5. Summary

The development of North American jet superpositions is conceptualized by Winters and Martin (2017) and Winters et al. (2020) as the juxtaposition of a polar cyclonic and tropical anticyclonic PV anomaly within the upper troposphere. This juxtaposition leads to the addition of the nondivergent circulations induced by each PV anomaly and the development of strong wind speeds at the location of jet superposition. Once the respective PV anomalies are juxtaposed, vertical motion within the near-jet environment contributes substantially to the development of a steep, single-step tropopause structure (Winters and Martin 2016, 2017; Handlos and Martin 2016; Winters et al. 2020). The influence of vertical motion during the development of jet superpositions motivates two analyses performed on jet superposition events in this study. First, this study utilizes piecewise QGPV inversion to quantify the relative influence of polar cyclonic and tropical anticyclonic PV anomalies on the production of vertical motion

←

in which $\omega_a > 0.5$ dPa s^{-1} (e.g., blue shading in Fig. 6b) is shown in green on the left-hand side of the plot. The components of the area-averaged ω_a ascent and descent that can be attributed to ω_s and ω_n are indicated by the blue and red contours, respectively. The gray shading highlights the total area (in 10^6 km^2) of ω_a ascent or descent on each isobaric level that was used to calculate the area-averaged ω_a (e.g., the total area of green or blue shading at 500 hPa in Fig. 6b). (b) As in (a), but for eastern subtropical dominant jet superpositions. (c) As in (a), but for western subtropical dominant jet superpositions.

within the near-jet environment. Second, the **Q** vector is partitioned into an along-isotherm $\mathbf{Q}_s$ and across-isotherm $\mathbf{Q}_n$ component to quantify the extent to which vertical motion in the near-jet environment is associated with synoptic-scale waves or frontal circulations in the vicinity of the jet, respectively.

The present study reveals that the QG vertical motion in the vicinity of polar dominant, eastern subtropical dominant, and western subtropical dominant jet superpositions is associated predominantly with the geostrophic wind induced by polar cyclonic QGPV anomalies and, in particular, the interactions between that geostrophic wind field with the mean temperature pattern and the perturbation temperature pattern associated with polar cyclonic QGPV anomalies. This result indicates that polar cyclonic QGPV anomalies are essential to the jet superposition process from the standpoint that their associated vertical-motion patterns contribute substantially to the production of a steep, single-step tropopause structure during the three jet superposition event types considered in this study. The strong influence of polar cyclonic QGPV anomalies on the development of jet superposition events complements prior case study work highlighting the substantial impact of coherent tropopause disturbances on the evolution of baroclinic waves at middle latitudes (e.g., Davis and Emanuel 1991; Hakim et al. 1996; Wandishin et al. 2000; Pyle et al. 2004; Winters and Martin 2017), and motivates future work to better understand the large-scale flow patterns that support the transport of polar cyclonic QGPV anomalies toward middle latitudes. This avenue of future work may be particularly effective in gauging the relative likelihood for the development of a jet superposition within an operational forecasting environment.

While the QG vertical motion in the vicinity of polar dominant, eastern subtropical dominant, and western subtropical dominant jet superpositions is associated primarily with the geostrophic wind induced by polar cyclonic QGPV anomalies, the QG vertical motion associated with the mid and upper-tropospheric baroclinicity induced by tropical anticyclonic QGPV anomalies is nonnegligible. Specifically, the presence of tropical anticyclonic QGPV anomalies in the vicinity of eastern and western subtropical dominant jet superpositions strengthens the mid and upper-tropospheric temperature gradient, such that the interaction between the geostrophic wind induced by polar cyclonic QGPV anomalies with the strengthened temperature gradient contributes to the production of QG vertical motion during these aforementioned jet superpositions. This particular interaction suggests that tropical anticyclonic QGPV anomalies, which can result from the cumulative effects of latent heating in the middle troposphere and/or the poleward transport of tropical low-PV upper-tropospheric air, do not impact the production of QG vertical motion via their induced geostrophic wind fields, but rather through their influence on the strength of the mid and upper-tropospheric baroclinicity. The contribution from tropical anticyclonic QGPV anomalies to the structure of the upper-tropospheric baroclinicity and to jet streak intensification has also been noted as part of prior work on rapidly deepening surface cyclones (e.g., Reed et al. 1993; Davis et al. 1996; Morgan and Nielsen-Gammon 1998) and recurving tropical cyclones (e.g., Riemer et al. 2008; Riemer and Jones 2010; Grams et al. 2011, 2013; Archambault et al. 2013; Grams and Archambault 2016).

Use of the **Q**-vector form of the QG–ω equation to partition the QG vertical motion into an along-isotherm component ω_s and an across-isotherm component ω_n provides additional insight into the character of QG vertical motion in the vicinity of jet superpositions. In particular, ω_s dominates the QG vertical-motion pattern during polar dominant events. The dominance of ω_s in the vicinity of upper-level jet front systems has also been observed within individual case studies (e.g., Pyle et al. 2004; Martin 2014). In the context of the present study, the dominance of ω_s implies that an amplified upper-tropospheric flow pattern during polar dominant events contributes substantially to the production of QG vertical motion within the near-jet environment and the formation of a steep, single-step tropopause structure during those events.

The ω_s pattern also dominates the QG vertical-motion pattern during eastern and western subtropical dominant events, but not to the same degree as during polar dominant events. Namely, the upper-tropospheric flow patterns during both eastern and western subtropical dominant events exhibit reduced amplitude compared to polar dominant events, which may explain the smaller contribution from ω_s to the QG vertical motion during both subtropical dominant event types. Additionally, eastern subtropical dominant events feature a larger relative contribution from ω_n to the QG vertical motion compared to polar and western subtropical dominant events. The larger relative contribution from ω_n during eastern subtropical dominant events suggests that frontal circulations in the vicinity of the jet have a stronger relative influence on the production of QG vertical motion during eastern subtropical dominant events compared to polar and western subtropical dominant events. Therefore, the **Q**-vector partition utilized in this study reveals that the dynamical mechanisms responsible for the production of QG vertical motion in the vicinity of jet superpositions vary in relative importance depending on the location of jet superposition.

Acknowledgments. This work was supported by the National Science Foundation through an AGS Postdoctoral Research Fellowship (AGS-1624316) held at the University at Albany, State University of New York by ACW. The authors thank David M. Schultz, Alicia M. Bentley, and two anonymous reviewers for their constructive comments throughout the review process.

Data availability statement. The CFSR dataset used in this study is publicly available from the Research Data Archive at NCAR (https://doi.org/10.5065/D69K487J). Data describing the jet superposition events utilized in this study are archived at the University of Colorado Boulder (https://doi.org/10.25810/tscc-2k05). All computer programs written to perform the data analysis are available from the first author upon request.

REFERENCES

Agusti-Panareda, A., C. D. Thorncroft, G. C. Craig, and S. L. Gray, 2004: The extratropical transition of Hurricane Irene (1999): A potential-vorticity perspective. *Quart. J. Roy. Meteor. Soc.*, **130**, 1047–1074, https://doi.org/10.1256/qj.02.140.

Ahmadi-Givi, F., G. C. Craig, and R. S. Plant, 2004: The dynamics of a midlatitude cyclone with very strong latent-heat release. *Quart. J. Roy. Meteor. Soc.*, **130**, 295–323, https://doi.org/10.1256/qj.02.226.

Archambault, H. M., L. F. Bosart, D. Keyser, and J. M. Cordeira, 2013: A climatological analysis of the extratropical flow response to recurving western North Pacific tropical cyclones. *Mon. Wea. Rev.*, **141**, 2325–2346, https://doi.org/10.1175/MWR-D-12-00257.1.

Black, R. X., and R. M. Dole, 1993: The dynamics of large-scale cyclogenesis over the North Pacific Ocean. *J. Atmos. Sci.*, **50**, 421–442, https://doi.org/10.1175/1520-0469(1993)050<0421:TDOLSC>2.0.CO;2.

Breeden, M., and J. E. Martin, 2018: Analysis of the initiation of an extreme North Pacific jet retraction using piecewise tendency diagnosis. *Quart. J. Roy. Meteor. Soc.*, **144**, 1895–1913, https://doi.org/10.1002/qj.3388.

——, and ——, 2019: Evidence for nonlinear processes in fostering a North Pacific jet retraction. *Quart. J. Roy. Meteor. Soc.*, **145**, 1559–1570, https://doi.org/10.1002/qj.3512.

Cavallo, S. M., and G. J. Hakim, 2009: Potential vorticity diagnosis of a tropopause polar cyclone. *Mon. Wea. Rev.*, **137**, 1358–1371, https://doi.org/10.1175/2008MWR2670.1.

——, and ——, 2010: Composite structure of tropopause polar cyclones. *Mon. Wea. Rev.*, **138**, 3840–3857, https://doi.org/10.1175/2010MWR3371.1.

——, and ——, 2012: Radiative impact on tropopause polar vortices over the Arctic. *Mon. Wea. Rev.*, **140**, 1683–1702, https://doi.org/10.1175/MWR-D-11-00182.1.

——, and ——, 2013: Physical mechanisms of tropopause polar vortex intensity change. *J. Atmos. Sci.*, **70**, 3359–3373, https://doi.org/10.1175/JAS-D-13-088.1.

Charney, J. G., and M. E. Stern, 1962: On the stability of internal baroclinic jets in a rotating atmosphere. *J. Atmos. Sci.*, **19**, 159–172, https://doi.org/10.1175/1520-0469(1962)019<0159:OTSOIB>2.0.CO;2.

Christenson, C. E., J. E. Martin, and Z. J. Handlos, 2017: A synoptic climatology of Northern Hemisphere, cold season polar and subtropical jet superposition events. *J. Climate*, **30**, 7231–7246, https://doi.org/10.1175/JCLI-D-16-0565.1.

Davis, C. A., 1992a: A potential vorticity diagnosis of the importance of initial structure and condensational heating in observed cyclogenesis. *Mon. Wea. Rev.*, **120**, 2409–2428, https://doi.org/10.1175/1520-0493(1992)120<2409:APVDOT>2.0.CO;2.

——, 1992b: Piecewise potential vorticity inversion. *J. Atmos. Sci.*, **49**, 1397–1411, https://doi.org/10.1175/1520-0469(1992)049<1397:PPVI>2.0.CO;2.

——, and K. A. Emanuel, 1991: Potential vorticity diagnostics of cyclogenesis. *Mon. Wea. Rev.*, **119**, 1929–1953, https://doi.org/10.1175/1520-0493(1991)119<1929:PVDOC>2.0.CO;2.

——, E. Donall Grell, and M. A. Shapiro, 1996: The balanced dynamical nature of a rapidly intensifying oceanic cyclone. *Mon. Wea. Rev.*, **124**, 3–26, https://doi.org/10.1175/1520-0493(1996)124<0003:TBDNOA>2.0.CO;2.

Fröhlich, L., P. Knippertz, A. H. Fink, and E. Hohberger, 2013: An objective climatology of tropical plumes. *J. Climate*, **26**, 5044–5060, https://doi.org/10.1175/JCLI-D-12-00351.1.

Grams, C. M., and H. M. Archambault, 2016: The key role of diabatic outflow in amplifying the midlatitude flow: A representative case study of weather systems surrounding western North Pacific extratropical transition. *Mon. Wea. Rev.*, **144**, 3847–3869, https://doi.org/10.1175/MWR-D-15-0419.1.

——, and Coauthors, 2011: The key role of diabatic processes in modifying the upper- tropospheric wave guide: A North Atlantic case-study. *Quart. J. Roy. Meteor. Soc.*, **137**, 2174–2193, https://doi.org/10.1002/qj.891.

——, S. C. Jones, C. A. Davis, P. A. Harr, and M. Weissmann, 2013: The impact of Typhoon Jangmi (2008) on the midlatitude flow. Part I: Upper-level ridgebuilding and modification of the jet. *Quart. J. Roy. Meteor. Soc.*, **139**, 2148–2164, https://doi.org/10.1002/qj.2091.

Hakim, G. J., 2000: Climatology of coherent structures on the extratropical tropopause. *Mon. Wea. Rev.*, **128**, 385–406, https://doi.org/10.1175/1520-0493(2000)128<0385:COCSOT>2.0.CO;2.

——, D. Keyser, and L. F. Bosart, 1996: The Ohio Valley wave-merger cyclogenesis event of 25–26 January 1978. Part II: Diagnosis using quasigeostrophic potential vorticity inversion. *Mon. Wea. Rev.*, **124**, 2176–2205, https://doi.org/10.1175/1520-0493(1996)124<2176:TOVWMC>2.0.CO;2.

Handlos, Z. J., and J. E. Martin, 2016: Composite analysis of large-scale environments conducive to west Pacific polar/subtropical jet superposition. *J. Climate*, **29**, 7145–7165, https://doi.org/10.1175/JCLI-D-16-0044.1.

Hecht, C. W., and J. M. Cordeira, 2017: Characterizing the influence of atmospheric river orientation and intensity on precipitation distributions over North Coastal California. *Geophys. Res. Lett.*, **44**, 9048–9058, https://doi.org/10.1002/2017GL074179.

Holopainen, E. O., and J. Kaurola, 1991: Decomposing the atmospheric flow using potential vorticity framework. *J. Atmos. Sci.*, **48**, 2614–2625, https://doi.org/10.1175/1520-0469(1991)048<2614:DTAFUP>2.0.CO;2.

Hoskins, B. J., and M. A. Pedder, 1980: The diagnosis of mid-latitude synoptic development. *Quart. J. Roy. Meteor. Soc.*, **106**, 707–719, https://doi.org/10.1002/qj.49710645004.

——, I. Draghici, and H. C. Davies, 1978: A new look at the ω-equation. *Quart. J. Roy. Meteor. Soc.*, **104**, 31–38, https://doi.org/10.1002/qj.49710443903.

——, M. E. McIntyre, and A. W. Robertson, 1985: On the use and significance of isentropic potential vorticity maps. *Quart. J. Roy. Meteor. Soc.*, **111**, 877–946, https://doi.org/10.1002/qj.49711147002.

Iskenderian, H., 1995: A 10-year climatology of Northern Hemisphere tropical cloud plumes and their composite flow patterns. *J. Climate*, **8**, 1630–1637, https://doi.org/10.1175/1520-0442(1995)008<1630:AYCONH>2.0.CO;2.

Kenyon, J. S., D. Keyser, L. F. Bosart, and M. S. Evans, 2020: The motion of mesoscale snowbands in northeast U.S. winter storms. *Wea. Forecasting*, **35**, 83–105, https://doi.org/10.1175/WAF-D-19-0038.1.

Keyser, D., and M. A. Shapiro, 1986: A review of the structure and dynamics of upper-level frontal zones. *Mon. Wea. Rev.*, **114**, 452–499, https://doi.org/10.1175/1520-0493(1986)114<0452:AROTSA>2.0.CO;2.

——, M. J. Reeder, and R. J. Reed, 1988: A generalization of Petterssen's frontogenesis function and its relation to the forcing of vertical motion. *Mon. Wea. Rev.*, **116**, 762–781, https://doi.org/10.1175/1520-0493(1988)116<0762:AGOPFF>2.0.CO;2.

——, B. D. Schmidt, and D. G. Duffy, 1992: Quasigeostrophic vertical motions diagnosed from along- and cross-isentrope

components of the Q vector. *Mon. Wea. Rev.*, **120**, 731–741, https://doi.org/10.1175/1520-0493(1992)120<0731:QVMDFA>2.0.CO;2.

Koteswaram, P., 1953: An analysis of the high tropospheric wind circulation over India in winter. *Indian J. Meteor. Geophys.*, **4**, 13–21.

——, and S. Parthasarathy, 1954: The mean jet stream over Indian in the pre-monsoon and post-monsoon seasons and vertical motions associated with subtropical jet streams. *Indian J. Meteor. Geophys.*, **5**, 138–156.

Krishnamurti, T. N., 1961: The subtropical jet stream of winter. *J. Meteor.*, **18**, 172–191, https://doi.org/10.1175/1520-0469(1961)018<0172:TSJSOW>2.0.CO;2.

Lang, A. A., and J. E. Martin, 2010: The influence of rotational frontogenesis and its associated shearwise vertical motion on the development of an upper-level front. *Quart. J. Roy. Meteor. Soc.*, **136**, 239–252, https://doi.org/10.1002/qj.551.

——, and ——, 2012: The structure and evolution of lower stratospheric frontal zones. Part I: Examples in northwesterly and southwesterly flow. *Quart. J. Roy. Meteor. Soc.*, **138**, 1350–1365, https://doi.org/10.1002/qj.843.

——, and ——, 2013: The structure and evolution of lower stratospheric frontal zones. Part II: The influence of tropospheric ascent on lower stratospheric frontal development. *Quart. J. Roy. Meteor. Soc.*, **139**, 1798–1809, https://doi.org/10.1002/qj.2074.

Lee, S., and H.-K. Kim, 2003: The dynamical relationship between subtropical and eddy-driven jets. *J. Atmos. Sci.*, **60**, 1490–1503, https://doi.org/10.1175/1520-0469(2003)060<1490:TDRBSA>2.0.CO;2.

Loewe, F., and V. Radok, 1950: A meridional aerological cross section in the southwest Pacific. *J. Meteor.*, **7**, 58–65, https://doi.org/10.1175/1520-0469(1950)007<0058:AMACSI>2.0.CO;2.

Martin, J. E., 1999: Quasigeostrophic forcing of ascent in the occluded sector of cyclones and the trowal airstream. *Mon. Wea. Rev.*, **127**, 70–88, https://doi.org/10.1175/1520-0493(1999)127<0070:QFOAIT>2.0.CO;2.

——, 2006: The role of shearwise and transverse quasigeostrophic vertical motions in the midlatitude cyclone life cycle. *Mon. Wea. Rev.*, **134**, 1174–1193, https://doi.org/10.1175/MWR3114.1.

——, 2014: Quasi-geostrophic diagnosis of the influence of vorticity advection on the development of upper level jet-front systems. *Quart. J. Roy. Meteor. Soc.*, **140**, 2658–2671, https://doi.org/10.1002/qj.2333.

Mohri, K., 1953: On the fields of wind and temperature over Japan and adjacent waters during winter of 1950–1951. *Tellus*, **5**, 340–358, https://doi.org/10.3402/tellusa.v5i3.8582.

Morgan, M. C., and J. W. Nielsen-Gammon, 1998: Using tropopause maps to diagnose midlatitude weather systems. *Mon. Wea. Rev.*, **126**, 2555–2579, https://doi.org/10.1175/1520-0493(1998)126<2555:UTMTDM>2.0.CO;2.

Namias, J., and P. F. Clapp, 1949: Confluence theory of the high tropospheric jet stream. *J. Meteor.*, **6**, 330–336, https://doi.org/10.1175/1520-0469(1949)006<0330:CTOTHT>2.0.CO;2.

Newton, C. W., 1954: Frontogenesis and frontolysis as a three-dimensional process. *J. Meteor.*, **11**, 449–461, https://doi.org/10.1175/1520-0469(1954)011<0449:FAFAAT>2.0.CO;2.

Nielsen-Gammon, J. W., and R. J. Lefevre, 1996: Piecewise tendency diagnosis of dynamical processes governing the development of an upper-tropospheric mobile trough. *J. Atmos. Sci.*, **53**, 3120–3142, https://doi.org/10.1175/1520-0469(1996)053<3120:PTDODP>2.0.CO;2.

Palmén, E., and C. W. Newton, 1948: A study of the mean wind and temperature distribution in the vicinity of the polar front in winter. *J. Meteor.*, **5**, 220–226, https://doi.org/10.1175/1520-0469(1948)005<0220:ASOTMW>2.0.CO;2.

——, and ——, 1969: *Atmospheric Circulation Systems: Their Structure and Physical Interpretation*. Academic Press, 603 pp.

Pyle, M. E., D. Keyser, and L. F. Bosart, 2004: A diagnostic study of jet streaks: Kinematic signatures and relationship to coherent tropopause disturbances. *Mon. Wea. Rev.*, **132**, 297–319, https://doi.org/10.1175/1520-0493(2004)132<0297:ADSOJS>2.0.CO;2.

Reed, R. J., Y.-H. Kuo, and S. Low-Nam, 1993: An adiabatic simulation of the ERICA IOP 4 Storm: An example of quasi-ideal frontal cyclone development. *Mon. Wea. Rev.*, **122**, 2688–2708, https://doi.org/10.1175/1520-0493(1994)122<2688:AASOTE>2.0.CO;2.

Riehl, H., 1962: Jet streams of the atmosphere. Tech. Rep. 32, Dept. of Atmospheric Science, Colorado State University, Fort Collins, CO, 117 pp.

Riemer, M., and S. C. Jones, 2010: Downstream impact of tropical cyclones on a developing baroclinic wave in idealized scenarios of extratropical transition. *Quart. J. Roy. Meteor. Soc.*, **136**, 617–637, https://doi.org/10.1002/qj.605.

——, ——, and C. A. Davis, 2008: The impact of extratropical transition on the downstream flow: An idealized modelling study with a straight jet. *Quart. J. Roy. Meteor. Soc.*, **134**, 69–91, https://doi.org/10.1002/qj.189.

Robinson, W. A., 1988: Analysis of LIMS data by potential vorticity inversion. *J. Atmos. Sci.*, **45**, 2319–2342, https://doi.org/10.1175/1520-0469(1988)045<2319:AOLDBP>2.0.CO;2.

Roundy, P. E., K. MacRitchie, J. Asuma, and T. Melino, 2010: Modulation of the global atmospheric circulation by combined activity in the Madden–Julian Oscillation and the El Niño–Southern Oscillation during boreal winter. *J. Climate*, **23**, 4045–4059, https://doi.org/10.1175/2010JCLI3446.1.

Saha, S., and Coauthors, 2010: The NCEP Climate Forecast System Reanalysis. *Bull. Amer. Meteor. Soc.*, **91**, 1015–1057, https://doi.org/10.1175/2010BAMS3001.1.

Sanders, F., and B. J. Hoskins, 1990: An easy method for estimation of Q-vectors from weather maps. *Wea. Forecasting*, **5**, 346–353, https://doi.org/10.1175/1520-0434(1990)005<0346:AEMFEO>2.0.CO;2.

Schultz, D. M., and C. A. Doswell III, 1999: Conceptual models of upper-level frontogenesis in south-westerly and north-westerly flow. *Quart. J. Roy. Meteor. Soc.*, **125**, 2535–2562, https://doi.org/10.1002/qj.49712555910.

Shapiro, M. A., and D. Keyser, 1990: Fronts, jet streams, and the tropopause. *Extratropical Cyclones: The Erik Palmén Memorial Volume*, C. Newton and E. O. Holopainen, Eds., Amer. Meteor. Soc., 167–191.

Son, S.-W., and S. Lee, 2005: The response of westerly jets to thermal driving in a primitive equation model. *J. Atmos. Sci.*, **62**, 3741–3757, https://doi.org/10.1175/JAS3571.1.

Starr, V. P., 1948: An essay on the general circulation of the earth's atmosphere. *J. Meteor.*, **5**, 39–43, https://doi.org/10.1175/1520-0469(1948)005<0039:AEOTGC>2.0.CO;2.

Sutcliffe, R. C., and J. K. Bannon, 1954: Seasonal changes in the upper-air conditions in the Mediterranean Middle East area. *Proc. Int. Association of Meteorology*, Rome, Italy, International Union of Geodesy and Geophysics, 322–334.

Thorpe, A. J., 1985: Diagnosis of balanced vortex structure using potential vorticity. *J. Atmos. Sci.*, **42**, 397–406, https://doi.org/10.1175/1520-0469(1985)042<0397:DOBVSU>2.0.CO;2.

Uccellini, L. W., and P. J. Kocin, 1987: The interaction of jet streak circulations during heavy snow events along the East Coast of the United States. *Wea. Forecasting*, **2**, 289–308, https://doi.org/10.1175/1520-0434(1987)002<0289:TIOJSC>2.0.CO;2.

Wandishin, M. S., J. W. Nielsen-Gammon, and D. Keyser, 2000: A potential vorticity diagnostic approach to upper-level frontogenesis within a developing baroclinic wave. *J. Atmos. Sci.*, **57**, 3918–3938, https://doi.org/10.1175/1520-0469(2001)058<3918:APVDAT>2.0.CO;2.

Winters, A. C., and J. E. Martin, 2014: The role of a polar/subtropical jet superposition in the May 2010 Nashville flood. *Wea. Forecasting*, **29**, 954–974, https://doi.org/10.1175/WAF-D-13-00124.1.

——, and ——, 2016: Synoptic and mesoscale processes supporting vertical superposition of the polar and subtropical jets in two contrasting cases. *Quart. J. Roy. Meteor. Soc.*, **142**, 1133–1149, https://doi.org/10.1002/qj.2718.

——, and ——, 2017: Diagnosis of a North American polar–subtropical jet superposition employing piecewise potential vorticity inversion. *Mon. Wea. Rev.*, **145**, 1853–1873, https://doi.org/10.1175/MWR-D-16-0262.1.

——, D. Keyser, L. F. Bosart, and J. E. Martin, 2020: Composite synoptic-scale environments conducive to North American polar–subtropical jet superposition events. *Mon. Wea. Rev.*, **148**, 1987–2008, https://doi.org/10.1175/MWR-D-19-0353.1.

Yeh, T. C., 1950: The circulation of the high troposphere over China in the winter of 1945–46. *Tellus*, **2**, 173–183, https://doi.org/10.3402/tellusa.v2i3.8548.